

A spatio-temporally constrained injection rate threshold for the mitigation of induced seismicity

By
© 2019

Andrew M. Hollenbach
B.A., University of Kansas, 2008

Submitted to the graduate degree program in the Department of Geology and the Graduate Faculty of the University of Kansas in partial fulfillment of the requirements for the degree
Master of Science.

Chair: Dr. George Tsoflias

Co-Chair: Dr. Tandin Bidgoli

Dr. Evan Franseen

Date Defended:

05/13/2019

The thesis committee for Andrew M. Hollenbach certifies that this
is the approved version of the following thesis:

A spatio-temporally constrained injection rate threshold for the
mitigation of induced seismicity

Chair: Dr. George Tsoflias

Co-Chair: Dr. Tandin Bidgoli

Date Approved:

08/12/2019

Abstract

The Cambrian-Ordovician Arbuckle Group is the primary disposal zone for Underground Injection Control (UIC) Class I and II wells across much of the U.S. midcontinent. Increases in wastewater disposal into the Arbuckle Group, linked with production from water-rich unconventional plays, is the inferred cause of a more than 40-fold increase in seismicity. Wastewater injection-induced seismicity has incited concerns about its potential impact on health and infrastructure, resulting in more than a decade of research on the subject. Nevertheless, mitigating earthquakes is a challenge for oil and gas operators and the regulatory community because a comprehensive understanding of operational factors (e.g., well spacing, injection rates, pore pressure diffusion in the Arbuckle and crystalline basement, etc.) and their relationship with seismicity is lacking. This study compares seismic events of magnitude 2.5+ with injection data from 4,366 brine disposal wells (Class 2) and 49 industrial waste wells (Class 1), from 2010 to 2017. A bi-variate Kernel Density Estimation method in R statistical software is used to construct a node lattice across the mapped data, and objectively compare the injected volumes, well densities, and earthquakes within a given radius from each node. The spatial scale of the analysis is varied by adjustment of the node lattice. The method identifies areas where the correlation between seismicity and nearby Arbuckle Group injection volumes are high, and also identifies areas where such a correlation appears to be diminished, or absent. The method tracks spatial distribution of injection volumes and seismicity, and can be used to monitor specific areas-of-interest or concern over time. The results can be referenced to inform rate-reduction calculations at the operational level.

Acknowledgements

There are many people who have helped me to this milestone. I am thankful to Dr. Tandis Bidgoli for a multitude of reasons, but primarily am grateful to have had an excellent advisor give me this opportunity and help me become a better scientist. I am also thankful to my other committee members, Dr. George Tsoflias and Dr. Evan Franseen, who have been a great source of knowledge and feedback. I owe thanks to Dr. Jennifer Roberts, Dr. Anthony Walton, Dr. Diane Kamola, and Dr. Douglas Walker for introducing me to geology and pushing me to build a strong foundation.

I owe many thanks to my parents and siblings who have each impacted my life immeasurably. I am, however, most thankful for my wife, Jennifer, whose brilliance, energy, and curiosity inspires me every day.

Table of Contents

Table of Contents	v
Table of Figures	vi
I Introduction	1
II Background	4
III Available Data	5
IV Methods	8
KDE Method	8
Well Inclusion Radius Method	10
V Results	11
KDE	11
Well Inclusion Radius Results	13
VI Discussion	14
Limitations	16
VII Conclusions	17
VIII References	19
Appendix:	30

Table of Figures

Figure 1: Study map.....	24
Figure 2: Top-of Arbuckle Group structure contour map.....	25
Figure 3: Spatially-averaged surface density of the injected volume	26
Figure 4: Spatio-temporal linearity of induced seismicity.....	27
Figure 5: Spatially tracking injected volumes, well-count, and seismicity over time	28
Figure 6: Earthquakes occurring within 40 km of each injection well by year	29

I Introduction

Earthquakes are increasingly occurring in low strain-rate intraplate settings (Ellsworth, 2013; Foulger et al., 2018; Weingarten et al., 2015). The risks associated with such unanticipated seismicity have spurred research into identifying possible anthropogenic causes (Ellsworth, 2013; Foulger et al., 2018, McGarr, 2014). Industrial operations cause earthquakes in a variety of ways—namely, through the injection or storage of fluids, the withdrawal of fluids, subsurface solution mining, and reservoir stimulation procedures (Deichmann & Giardini, 2009; Ellsworth, 2013; Foulger et al., 2018; Maghsoudi et al., 2018; McGarr, 2014; Shapiro, 2015; Suckale, 2010).

Injection-induced seismicity occurs all over the world (Foulger et al., 2018; McGarr et al., 2002; Segall & Lu, 2015; van Eck et al., 2006). In the United States, the development of unconventional water-rich oil reserves has led to an increase of injection-induced earthquakes occurring in places with low seismicity rates like Arkansas, Texas, Ohio, Colorado, New Mexico, Oklahoma, and Kansas (Ake et al., 2005; Frohlich et al., 2014; Gupta, 2013; Hornbach et al., 2015; Horton, 2012; Keranen et al., 2014; King et al., 2014; McGarr, 2014; Petersen et al., 2018; Walsh & Zoback, 2016). Induced seismicity also occurs in tectonically active places like California, where spatial and temporal correlations are an essential component of determining whether the earthquakes were anthropogenic in origin or occurring as a part of natural tectonic processes (Goebel et al., 2015).

The leading physical model for injection-induced seismicity is that pore-pressure diffusion, responding to deep and high rate fluid injection, perturbs critically stressed basement faults (Ellsworth, 2013; Nolte et al., 2017; Weingarten et al., 2015; Yeck et al., 2016; Zhang et al.,

2013). The faults are mechanically triggered when induced pressure changes cause an adjustment of the poroelastic Coloumb stress-state, resulting in slip (Chang & Segall, 2016; Hearn et al., 2018; Segall & Lu, 2015; Sumy et al., 2014). The pore-pressure diffusion model has been tested through numerical simulation and repeatedly validated, albeit with each model requiring assumptions with respect to initial stress and pore pressure conditions (Ellsworth, 2013, Khademian et al., 2018, Norbeck & Rubinstein, 2018).

In Kansas and Oklahoma, the increase in earthquake frequency is coincident with an increase in the volume of waste-water disposed (Andrews, 2015; Ellsworth, 2013; Keranen et al., 2014; Rubinstein et al., 2018; Schoenball et al., 2018; Walsh & Zoback, 2015). Investigators have performed hazard assessments (Andrews, 2015; Eaton & Igonin, 2018; Langenbruch et al., 2018; Petersen et al., 2018; Walsh & Zoback, 2016), measured geophysical and geomechanical stress states (Alt & Zoback, 2017; Chang & Segall, 2016; Kroll et al., 2017; Nolte et al., 2017; Norbeck & Rubinstein, 2018), identified faults (Mcnamara et al., 2015; Schoenball et al., 2018; Schwab et al., 2017)), and determined stress states (Alt & Zoback, 2017; Fan et al., 2016; Sumy et al., 2014). These efforts have recently culminated in both validation of the pore-pressure diffusion model through numerical simulation (Norbeck & Rubinstein, 2018; Langenbruch et al., 2018, 2016; Hearn et al., 2018; Choy et al., 2016) as well as recognition that earthquake probability increases with the square of the pressure rate (Langenbruch et al., 2018). This means that slow pressure increases translate to significantly lower earthquake probabilities (Langenbruch et al., 2018). Research in this area continues in Kansas and Oklahoma, with efforts to identify faults, develop hazard models and risk assessments, and obtain higher-resolution measurements of seismicity and injection for future study. Predicting the location, depth, frequency, and magnitude of seismicity involves a combination of hydrogeological analysis (e.g.

location of deep structural features) and investigation of waste-water disposal (the volume, rate, and location). Location-specific hydrogeological factors are first order controls on pore-pressure conditions (Yeck et al., 2016).

Although the previous research in this area is useful for understanding the phenomenon of induced-seismicity, studies to-date have also been complex, and have had limited practical applicability toward making informed rate-reduction decisions. In response to increased seismicity, both Kansas and Oklahoma have begun efforts to mitigate earthquake frequency and decrease the potential for a high magnitude event. In 2015, the Oklahoma Corporation Commission mandated significant volume reductions at higher volume wells, as well as the plugging back of the total depth of numerous wells (OCC, 2017). In 2015 and 2016, the Kansas Corporation Commission similarly mandated injection rate reductions at high volume wells (Feist Albrecht et al., 2015; Scott Emler et al., 2016). These measures along with commodity-price-driven reductions in oil and gas activity in the region have proved impactful, and seismicity has retreated from the peak-earthquake frequency recorded in 2014 (Langenbruch et al., 2016). The seismicity problem remains a concern, however, and operators and regulators working on the problem currently have few tools for making informed decisions despite nearly a decade of research.

Two simple geostatistical methods are presented here which may help operators and regulators identify at-risk areas, track such areas over time, and inform rate-reduction decisions to help mitigate the risk of inducing an earthquake. The methods are focused on evaluating the spatial and temporal correlation between injection volume and earthquake frequency.

The two methods spatially average and compare otherwise discrete and location-specific data. The first focuses on the spatial correlation between injection volume and earthquake frequency by varying the smoothing parameter (bandwidth) of a 2D multivariate Kernel Density Estimation (KDE) method. This distinguishes areas that have a strong correlation in contrast to areas where the correlation is absent or diminished. The second geostatistical method focuses on operational-level rate thresholds, and references development that can help guide rate-reduction calculations by varying the bandwidth of an inclusion area around each well and addressing per-well-volume (rate) considerations.

The results of this work both reinforce the importance of rate-reduction in areas experiencing seismicity (Langenbruch et al., 2018) as well as provide references and methods that can be used to help identify future at-risk areas, track the volumetric and seismicity changes occurring in those areas over time, and identify reduction-targets using simple statistics.

II Background

It is now recognized that injection into deep, fractured basal aquifers or crystalline basement can result in earthquakes (Hincks et al., 2018; Zhang et al., 2013). Such basal aquifers will remain important targets for the disposal of unwanted waste-water because multiple low-permeable seals and traps prevent waste-water stored at depth from migrating toward and contaminating shallow-water (J. E. Carr et al., 1984). For similar reasons, deep basal aquifers are also prospective targets for long-term storage of CO₂ (Benson & Cole, 2008; T. R. Carr et al., 2005; Schwab et al., 2017). In Kansas and Oklahoma, the Arbuckle Group is the basal aquifer and primary target for fluid disposal.

The seismicity problem in this area is complicated by the characteristics of the Arbuckle Group aquifer, such as the presence of fractures and faults, primary depositional fabrics, paleokarst, and diagenetic overprint (Franseen et al., 2004; Fritz et al., 2012). The Arbuckle Group is under-pressured, porous, and permeable, making it ideal for fluid disposal injection wells are typically completed in the shallow portion of the Arbuckle Group (often penetrating no more than 200 feet). The volume of fluid disposed into the Arbuckle Group has been increasing steadily since the early 1900s, and the reservoir has long been treated as effectively infinite. Recent, unconventional development of water-rich hydrocarbon resources has led to a sudden volumetric increase of disposal, with the associated disposal wells commonly situated in the Arbuckle Group.

The seismic hazard in Kansas and Oklahoma prior to 2013 was low. The sudden increase of seismicity beginning in 2013 and persisting into today was not anticipated, but mitigation has quickly become a priority. As injection volumes have declined and/or stabilized since 2014, both the frequency and magnitude of the seismicity has also declined. Previous research has provided insight into the phenomenon of induced seismicity (Langenbruch et al., 2018, Norbeck & Rubinstein, 2018, Yeck et al., 2016), but the hazard remains a concern, and there is yet to be a simple, intuitive, and cost-effective way to inform mitigation decision making. This study offers one possible approach to filling this void.

III Available Data

Datasets used for our spatiotemporal analysis are compiled from publicly available information of different vintages and collected from a variety of sources (e.g., United States Geological Survey, Kansas Geological Survey (KGS), Kansas Corporation Commission, Kansas

Department of Health and Environment, and Oklahoma Corporation Commission). The data include: (a) well locations and formation tops data; (b) annual injection volumes and related data (e.g., injection zone, permitted injection limits, etc.) for 4,415 injection wells comprised of 49 Class I (hazardous fluid disposal) injection wells and 4,366 Class II (disposal of waste-fluids co-produced with oil and gas) injection wells in the Arbuckle Group and deeper zones in Kansas and Oklahoma, from 2010 to 2017; and (c) earthquake data, covering the same period, including location, time, depth, and magnitude of M2.5+ events in Kansas and Oklahoma (Figure 1). The full suite of data is available in the supporting materials (Tables S1 and S2).

Kansas well locations and formation tops (stratigraphic well picks) were obtained from the KGS, which maintains an online repository of oil and gas information (KGS, 2019). Oklahoma top of Arbuckle Group and top of basement well picks were donated by Berexco, LLC.

The disposal volume data were compiled from three sources: 1) the KGS, which maintains a saltwater disposal well database from injection records reported to the Kansas Corporation Commission, the public entity responsible for regulating Class II injection wells in Kansas; 2) the Oklahoma Corporation Commission, the public entity responsible for regulating Class II injection wells in Oklahoma; and 3) the Kansas Department of Health and Environment, the public entity responsible for regulating Class I injection wells in Kansas. The data from these sources were collated into a single data-frame and standardized to a single cumulative annual injection volume for each year within the range of 2010 through 2016 (e.g. the annual sum of monthly-recorded volumes).

Disposal can occur in several geologic aquifers that are separated by low permeable hydraulic seals in a stacked system (J. E. Carr et al., 1984; Magoon & Dow, 1995; Zhang et al., 2013).

Induced seismicity in the basement is the result of injection into the basal sedimentary aquifer(s), as opposed to injection into one of the many overlying aquifers separated by seals (Zhang et al., 2013). Therefore, the disposal volume data were filtered to include only Arbuckle Group and basement injectors, where disposal volumes are thought to be in hydraulic communication with the faulted crystalline basement. Filtering to isolate deeper wells of interest also prevents accidental inclusion of enhanced-oil-recovery injection wells. There are many wells within the Arbuckle that have listed volumes, but the injection zone is unknown. In order to prevent exclusion of such wells, we developed a regional grid of the top-of-Arbuckle Group across Kansas and Oklahoma and filtered the data such that unknown wells must penetrate the Arbuckle surface (Figure 2) in order to be incorporated. The assumption is that if a well penetrates the Arbuckle surface, then the Arbuckle is the zone of injection. The Arbuckle grid was developed in PetraTM from 65,879 wells with data indicating the top of the Arbuckle Group.

Earthquake data were obtained from the US Geological Survey ANSS Comprehensive Earthquake Catalog (ComCat), an online catalog of earthquake source parameters including location, time, and magnitude (USGS, 2018). We include earthquakes in Kansas and Oklahoma with a magnitude larger than 2.5 occurring from 2010 through the first half of 2017. Seismic events with a magnitude of less than 2.5 were excluded from this study due to spatial (depth) uncertainties that arise from receiver locations relative to earthquake sources and the inherent difficulty of accurately recording low magnitude and low energy events. For this study, we use the full ComCat catalog, which includes foreshocks and aftershocks of several low- to moderate-magnitude events (e.g., Schoenball et al., 2018; Sumy et al., 2014). This decision was made because attempting to separate such events from mainshocks is difficult, particularly in areas of induced seismicity, and is reliant upon subjective algorithms

(Gardner & Knopoff, 1974; Langenbruch et al., 2018; Reasenber, 1985). A similar approach was taken by Langenbruch et al. (2018).

IV Methods

To investigate the spatial and temporal relationships between injection into the Arbuckle Group and seismic activity, we employ geostatistical analysis in RTM, an open-source language and environment capable of a wide variety of statistical and graphical analysis (R Core Team, 2017).

We use two approaches to spatially average the discrete and non-continuous point data (i.e., injection volumes at well locations and earthquake epicenters): (1) a kernel density estimation (KDE) method (Duong, 2007) and (2) a well inclusion radius method (Duong, 2007).

KDE Method

KDE was used to spatially average the datum stored at locally-discrete points (earthquake and well locations). KDE is commonly used for 1D spatial smoothing of histograms (Duong, 2001; Figure 5). There are many methods of KDE available, ranging in complexity and function (Cao et al., 1994; Deng & Wickham, 2011; Duong, 2007; Sheather, 2004). This study describes the steps to perform a relatively simple version of bi-directional KDE satisfactory for our intended purpose. The method projects well and earthquake point locations upon a two-dimensional grid imposed over the study area.

The variable values at each well are abstracted through spatial-averaging onto overlapping circles placed at the center of each grid intersection. The bandwidth, r , is adjusted to estimate the differences in linearity between variables at different spatial and temporal resolutions. The bandwidth also represents both the distance between the grid intersections and the radius of each overlapping circle (Figure 1). If the radius of the circle is made smaller than the distance

between the grid intersections, then there are data-gaps missing from the analysis.

Alternatively, if the radius of the circle becomes larger than the distance between the grid intersections, the output is weighted arbitrarily, with the result likely over-smoothed.

Using this method, the following enumerated steps are performed in R-Studio:

1. A lattice of points is constructed to form a flat grid across the project map, resulting in n points $i_1 \dots i_n$. Each point of the lattice is separated by the bandwidth, r (Figure 1).
2. At each point $i_1 \dots i_n$, a search radius of the same bandwidth (r) forms numerous overlapping circles, all with the same sized area ($A = \pi r^2$).
3. At each circle, calculate the sum volume (V) of the individual wells and the number of earthquakes. Total disposal volume (V) may be divided into the aforementioned areas (A) to yield an averaged surface density (density) of the injection volume ($D = V/A$).

The output data-frame contains the: 1) x-y locations of each circular area, 2) the total volume recorded within each circle, 3) volume density (i.e. total volume divided into the circular area, 4) number of Arbuckle injection wells, (5) well density (i.e. the number of wells divided into the circular area), (6) average volume-per-well within the circular area, and (7) number of earthquakes occurring within the circle. The number of rows in the output data-frame is fixed to the number of grid intersections. A higher bandwidth results in a coarser grid and fewer circles.

In order to evaluate the temporal correlation between injection volume and seismicity, the process is repeated but with 1-year of earthquake data that were staggered 3-months, 6-months, and 9-months behind the injection year. For example, injection volumes reported for

the year 2014 are compared to earthquakes that occur from April 1, 2014 to April 1, 2015 (considered a 3-month delay from injection).

To further evaluate the relationships, we filter the KDE results to include only seismically active areas (meaning at least one earthquake occurred within the circle), and we use linear regression to calculate the linearity of earthquake frequency as a function of disposal volume (Figure 4).

Well Inclusion Radius Method

The well inclusion radius method is similar to the KDE method in that circles are used to spatially average data at varying bandwidths, however injection data were not abstracted from the well locations. Instead, the circles spatially average the data around every injection well (i.e. an inclusion radius around each well). The total volume of injection, the number of wells, and the number of earthquakes occurring within the radius are recorded. The enumerated steps performed in RTM are as follows:

1. At each injection well, a search radius (r) forms circles that all have the same-sized area ($A = \pi r^2$).
2. At each circle, calculate the sum volume (V) of the individual wells, the number of earthquakes, and the number of wells. The total disposal volume (V) may be divided into the area (A) to yield an averaged density of the injection volume ($D = V/A$). The volume can also be divided by the number of wells to calculate the average volume-per-well within the circle.

The output data-frame has the same information as the KDE method and contains the: 1) x-y locations of each circular area (i.e. the well locations), 2) total disposal volume within each

circle, 3) volume density (i.e. total volume divided into the circular area, 4) number of Arbuckle injection wells, 5) well density (i.e. The number of wells divided into the circular area), 6) average volume-per-well within the circular area, and 7) the number of earthquakes occurring within the circle. The number of rows in the data-frame will be exactly the number of wells used for the study.

V Results

KDE

The KDE method simplifies the discretized volume data (discrete with respect to both the well locations and the injection volumes) by spatially averaging into overlapping circles. The result is the ability to contour the gridded output with normal techniques in order to visualize and compare the spatial-density of injection volume, earthquake frequency, and number of injection wells. As an example, Figure 3 was produced by deploying the KDE method at a 20 km bandwidth and contouring the output data-frame for each year. This involved determining the Volume Density (i.e. the spatially-averaged injection volume/area), and then super-imposing earthquake locations to visualize the spatial relationship between injection and seismicity.

Injection volumes increase in central Oklahoma and, most-notably, in north-central Oklahoma and south-central Kansas, from 2010 to 2014. The flare-up of seismicity across central-Oklahoma and into Kansas begins in 2013 and remains frequent, albeit decreased following the stabilization of injection volumes beginning in 2014.

We can quantify these observations by referencing the output data-frame used to build the figure, which numerically assigns a unique identifier to each area. Continuing with the 20 km bandwidth

example, and selecting area no. 648 of 1295, which is located in the heart of the volumetric increase in north-central Oklahoma (Alfalfa county), the cumulative volume (Bbls) into the $\pi(20 \text{ km})^2$ area from 2010 to 2017 is 1.6×10^7 , 5.1×10^7 , 1.1×10^8 , 2.1×10^8 , 2.4×10^8 , 2.5×10^8 , and 8.8×10^7 , for each year, respectively. Note the order of magnitude increase between 2010 and 2013, and a slight decline by 2017. The number of earthquakes experienced in the same area, occurring over the same period, is 1, 0, 0, 33, 84, 139, and 46. The same data is tabulated below for ease of review:

Example of tracking volume and seismicity of area no. 648

Year	2010	2011	2012	2013	2014	2015	2016
Annual Cumulative Volume (Bbls)	1.6×10^7	5.1×10^7	1.1×10^8	2.1×10^8	2.4×10^8	2.5×10^8	8.8×10^7
Number of Earthquakes	1	0	0	33	84	139	46

The KDE method was also used to investigate the quality of the correlation with respect to space and time. Figure 4 tabulates the linearity (R^2) of earthquake frequency as a function of volume for each year from 2010 to 2017 at various spatial and temporal bandwidths in areas that experienced at least one earthquake. Spatially, the linearity is strongest between 40 and 60 km, where the average measured R^2 for the entire 2010 to 2017 timeframe is .69 and .73, respectively. Temporally, the linearity is strongest when the earthquake data were not staggered behind the injection data. For example, at a 40 km bandwidth, the linearity of

earthquake frequency as a function of volume decreases from 0.7 to 0.4 when earthquake data is staggered behind injection volume data by three months.

Well Inclusion Radius Results

The well inclusion radius method was used to investigate the effect of injection rate (per-well-volumes) on earthquake frequency. To analyze the results, the output data-frame was plotted to 2D scatterplots developed using GGLOT in RTM (Figure 5). Each point on the plot represents a specific inclusion area around a specific well. The total injection volume and number of injection wells within the same area was plotted to the x- and y-axis, respectively. The points are colored according to a continuous color gradient reflective of the number of earthquakes occurring in the inclusion area. Figure 6 presents the corresponding map-locations of the points plotted in Figure 5.

Figure 5 reveals how injection-rates differ by location over time. At any spatial bandwidth, the points cluster into two recognizable domains that overlap in the lower volume and lower well count. At higher volumes (moving right along the plot) there exists a domain in which the number of injection wells increases concomitantly with injection volume (moving upward on the plot). The points in this domain are plotted gray (at lower bandwidths), indicating that they are not commonly seismically active, even after the onset of seismicity in 2013. Additionally, the highest injection rates remain relatively stable throughout the study period and do not show dramatic increases as seen in the second domain. The points in the second domain are commonly plotted red after the onset of seismicity in 2013, indicating that these areas are experiencing seismicity. The points plotted in this domain do show a dramatic increase of injection volume (moving right from 2010 to 2014) over the time frame.

The majority of the points (areas) on the plot congregate close to the origin and at lower injection volumes. We used a 1D kernel density estimation in the GGPUBR package of RTM (Kassambara, 2018) to elucidate the distribution of the results with respect to injection volumes, displayed in blue above each scatter-plot.

VI Discussion

There are areas where seismicity occurs without spatiotemporal correlation to injection volumes (identified as A and D on Figure 3). There are also areas—most notably the Central Kansas Uplift (CKU, area B on Figure 3) and south-central Kansas—where Arbuckle injection occurs without correlation to earthquake frequency (identified as B and C on Figure 3). Areas of poor correlation are interesting but not surprising; where correlation is absent, we can evoke alternative explanations.

The CKU (area B on Figure 3) does not correlate spatially to seismicity, but significant volumes of fluid are being disposed. Figure 5 reveals that the CKU area has typically more wells per unit-volume of disposed fluid. The lack of spatial correlation to seismicity in the CKU, and the higher number of injection wells, could lead the hypothesis that adding more injection wells, and decreasing the per-well-injection *as seen in the CKU* will mitigate seismicity. This would be incorrect, however, because: 1) the increased number of wells is a reflection of the oil cut, not of operators adding injection wells to mitigate a seismic threat; 2) oil in the CKU is primarily produced from the Arbuckle Group, meaning fluid production, followed by oil-water separation and reinjection of waste-water, would represent a *decrease* of total fluid volume; and 3) the CKU did not see a dramatic *increase* of injection volumes during the study period or prior to the onset of seismicity.

Area C of Figure 3 is interesting because there is little or no correlation to earthquake frequency at lower spatial bandwidths, despite a sharp increase of injection volume to the Arbuckle Group (not recycled, as in the case of the CKU). When the spatial bandwidth parameter is sufficiently high to span the distance between injection and seismicity, the correlation is reestablished. Using the KDE Method, we can measure the distances between the spatially-averaged circles and seismicity. If we compare the 2014 results for 20 km and 60 km in the vicinity of Area C, we find that at 20 km earthquakes (occurring to the southeast of C) are not averaged into the high-volume areas, but that at 60 kilometers the earthquakes are averaged and linearity is established. Area C is partly responsible for the apparent increase in overall linearity between 20 km and 40 km (Figure 4). The area is unique, and despite an order of magnitude increase in the injection volume, there has not been a high frequency of nearby earthquakes. One hypothesis is that Area C may be north-west and west of the slip on critically-stressed faults in the basement.

The kernel density estimation (1-D smoothing of a density histogram) of the calculated well inclusion radius injection volumes in Figure 5 (blue) reveal that a very small number of areas (at any bandwidth) are injecting at rates significantly higher than the majority. The methods and resulting references of this study can help operators determine if their well, or group of wells, are significantly contributing to the volume relative to surrounding fields—and if so, help establish rate-reduction targets. A direct and simple solution for operational decision-making regarding a specific location is to draw a 40 km circle around a well or point of concern, sum the injection volume occurring within that circle, count the number of injection wells, and then plot the area's position on Figure 5.

This study shows that in seismically active areas, at an assumed instantaneous response time, and at bandwidths between 20 km and 60 km, injection volume strongly correlates to earthquake

frequency. The spatial correlation at 60 km bandwidth or greater is typically high even as variance is not preserved, with the outcome heavily influenced by grid placement (fewer circles). In comparison, correlations at bandwidths of 20 km or smaller are typically low, variance is preserved, and the outcome is not dependent on grid placement (many circles). The differences in correlation between 20 km and 60 km also depend on specific wells and their respective distances to nearby seismicity, such as those areas identified in Figure 3. Temporally, the correlation between injection volume and earthquake frequency decreases when seismicity data were staggered behind the annual injection volumes, consistent with the observations of Langenbruch and Zoback, 2016. It is, however, difficult to investigate lag-times because injection volumes are reported as a single cumulative total, per-well, annually, which is an insufficient resolution for investigating a temporal lag-time period which spans months (less than one year). The results of this study indicate that higher correlations are obtained when assuming instantaneous fault activation (Figure 4).

There is not a single, injection volume threshold at which earthquakes are induced. However, area-specific rate-reduction targets can be identified using the simple, geostatistically-based methods described in this work.

Limitations

In employing the methods of this paper, the following limitations should be taken into consideration:

1. The KDE method inherently produces linearity. Results from this method of analysis should therefore be restricted to constraining spatiotemporal comparisons relative to the same

data, and not interpreted to mean that injection has direct linear correlation to earthquake frequency.

2. Extremely low and extremely high bandwidths are not useful. At low bandwidths, variance is preserved but correlation is poor. At high bandwidths, there are fewer areas to spatially average the data, and therefore translation of the grid will have a significant effect on the outcome. This fact can be useful for optimizing the bandwidth of spatial correlation that is too coarse at 80 km and too fine at 5 km.

3. 3-dimensional data were abstracted to a 2-dimensional plane. The majority of the earthquake hypocenters occur at depths greater than 1 km below injection, and horizontal pressure diffusion (e.g. along laterally continuous Arbuckle strata or a fault plane) is not considered. Therefore, at lower bandwidths there is a higher likelihood of no correlation to earthquakes that occur tens of kilometers adjacent in the x-y plane.

4. Injection volume data were reported by operators, and there are uncertainties related to how the data was collected and reported.

VII Conclusions

In some areas where seismicity occurs, there is a strong correlation between injection volume and earthquake frequency. In other areas the correlation is weak or absent, suggesting that a single, across-the-board rate threshold for induced seismicity does not exist, although location-specific mitigation targets can be identified. We find that a relatively small number of spatially-

averaged areas (at any spatial scale) increased injection volumes to an order of magnitude above historical volumetric highs, and that the same areas had corresponding increases of earthquake frequency.

The complexities associated with mitigation strategies for the problem of injection-induced seismicity can be simplified using simple geostatistical methods. The KDE method is effective for monitoring specific areas of concern without bias towards individual fields or wells. The Well-Inclusion-Radius Method is effective for investigating how a specific injection well, or a group of injection wells, is potentially contributing to the induced-seismicity problem and can inform rate-reduction calculations to minimize the seismic risk.

VIII References

- Ake, J., Mahrer, K., O'Connell, D., & Block, L. (2005, apr). Deep-Injection and Closely Monitored Induced Seismicity at Paradox Valley, Colorado. *Bulletin of the Seismological Society of America*, 95(2), 664–683. doi: 10.1785/0120040072
- Alt, R. C., & Zoback, M. D. (2017). In situ stress and active faulting in Oklahoma. *Bulletin of the Seismological Society of America*, 107(1). doi: 10.1785/0120160156
- Andrews, R. D. (2015). Statement on Oklahoma Seismicity. *Oklahoma Geological Survey, Circular 3*, 1–2.
- Barbour, A. J., Norbeck, J. H., & Rubinstein, J. L. (2017). The Effects of Varying Injection Rates in Osage County, Oklahoma, on the 2016 M w 5.8 Pawnee Earthquake. *Seismological Research Letters*, 88(4), 1040–1053. doi: 10.1785/0220170003
- Benson, S. M., & Cole, D. R. (2008). CO 2 Sequestration in Deep Sedimentary Formations. *Geoscience Elements*, 4, 325–331. doi: 10.2113/gselements.4.5.325
- Cao, R., Cuevas, A., & Gonzalez Manteiga, W. (1994, feb). A comparative study of several smoothing methods in density estimation. *Computational Statistics & Data Analysis*, 17(2), 153–176. doi: 10.1016/0167-9473(92)00066-Z
- Carr, J. E., McGovern, H. E., Gogel, T., & Doveton, J. H. (1984). *Geohydrology of and potential for fluid disposal in the Arbuckle aquifer in Kansas* (Tech. Rep.). Lawrence, Kansas: U.S. Geological Survey Open-File Report.
- Carr, T. R., Merriam, D. F., & Bartley, J. D. (2005). Use of relational databases to evaluate regional petroleum accumulation, groundwater flow, and CO2 sequestration in Kansas. *AAPG Bulletin*, 89(12), 1607–1627. doi: 10.1306/07190504086
- Chang, K. W., & Segall, P. (2016). Injection-induced seismicity on basement faults including poroelastic stressing. *Journal of Geophysical Research: Solid Earth*, 121(4), 2708–2726. doi: 10.1002/2015JB012561
- Choy, G. L., Rubinstein, J. L., Yeck, W. L., McNamara, D. E., Mueller, C. S., & Boyd, O. S. (2016). A Rare Moderate Sized M4.9 Earthquake in Kansas: Rupture Process of the Milan, Kansas, Earthquake of 12 November 2014 and Its Relationship to Fluid Injection. *Seismological Research Letters*, 87(6). doi: 10.1785/0220160100
- Deichmann, N., & Giardini, D. (2009). Earthquakes Induced by the Stimulation of an Enhanced Geothermal System below Basel (Switzerland). *Seismological Research Letters*, 80(5), 784–798. doi: 10.1785/gssrl.80.5.784
- Deng, H., & Wickham, H. (2011). *Density Estimation In R* (Tech. Rep. No. September). doi: 10.1016/S0040-4020(98)00814-X
- Duong, T. (2001). An introduction to kernel density estimation. In *Weatherburn lecture series for the department of mathematics and statistics* (pp. 1–4).
- Duong, T. (2007). Kernel Density Estimation and Kernel Discriminant Analysis for Multivariate Data in R. *Journal of Statistical Software*, 21(7).
- Eaton, D. W., & Igonin, N. (2018). What controls the maximum magnitude of injection-induced earthquakes? *The Leading Edge*, 37(2). doi: 10.1190/tle37020135.1
- Ellsworth, W. L. (2013). Injection-Induced Earthquakes. *Science*, 341(July), 1–7.
- Fan, Z., Eichhubl, P., & Gale, J. F. W. (2016). Geomechanical analysis of fluid injection and seismic fault slip for the Mw4.8 Timpson, Texas, earthquake sequence. *Journal of Geophysical Research: Solid Earth*, 121, 2798–2812. doi: 10.1002/2016JB012821

- Feist Albrecht, S., Scott Emler, J., & Apple, P. (2015). *Order Reducing Saltwater Injection Rates* (Tech. Rep.).
- Foulger, G. R., Wilson, M. P., Gluyas, J. G., Julian, B. R., & Davies, R. J. (2018). Global review of human-induced earthquakes. *Earth-Science Reviews*, 178. doi: 10.1016/j.earscirev.2017.07.008
- Franseen, E. K., Byrnes, A. P., Cansler, J. R., Steinhauff, D. M., & Carr, T. R. (2004). The Geology of Kansas Historical Aspects of Arbuckle. *Kansas Geological Survey Earth Sciences Bulletin*, 250(part 2), 1–43.
- Fritz, R., Medlock, P., Kuykendall, M. J., & Wilson, J. L. (2012). The Geology of the Arbuckle Group in the Midcontinent: Sequence Stratigraphy, Reservoir Development, and the Potential for Hydrocarbon Exploration. In J. Derby & R. Fritz (Eds.), *The great american carbonate bank: The geology and economic resources of the cambrian - ordovician sauk megasequence of laurentia* (98th ed., pp. 208–273). AAPG Memoir.
- Frohlich, C., Ellsworth, W. L., Brown, W. A., Brunt, M., Luetgert, J., MacDonald, T., & Walter, S. (2014). The 17 May 2012 M4.8 earthquake near Timpson, East Texas: An event possibly triggered by fluid injection. *Journal of Geophysical Research: Solid Earth*, 119, 1–13. doi: 10.1002/2013JB010755
- Gardner, J. K., & Knopoff, L. (1974, oct). Is the sequence of earthquakes in Southern California, with aftershocks removed, Poissonian? *Bulletin of the Seismological Society of America*, 64(5), 1363–1367
- Goebel, T. H., Hauksson, E., Aminzadeh, F., & Ampuero, J. P. (2015). An objective method for the assessment of fluid injection-induced seismicity and application to tectonically active regions in central California. *Journal of Geophysical Research: Solid Earth*, 120(10). doi: 10.1002/2015JB011895
- Gupta, H. K. (2013). Triggered earthquakes. In *Encyclopedia of earth sciences series*. doi: 10.1007/978-1-4020-4399-4 55
- Hearn, E. H., Koltermann, C., & Rubinstein, J. R. (2018). Numerical Models of Pore Pressure and Stress Changes Along Basement Faults Due to Wastewater Injection: Applications to the 2014 Milan, Kansas Earthquake. *Geochemistry, Geophysics, Geosystems*. doi: 10.1002/2017GC007194
- Hincks, T., Aspinall, W., Cooke, R., & Gernon, T. (2018, mar). Oklahoma’s induced seismicity strongly linked to wastewater injection depth. *Science (New York, N.Y.)*, 359(6381), 1251–1255. doi: 10.1126/science.aap7911
- Hornbach, M. J., Deshon, H. R., Ellsworth, W. L., Stump, B. W., Hayward, C., Frohlich, C., ... Luetgert, J. H. (2015). Causal factors for seismicity near Azle, Texas. *Nature Communications*, 6, 1–11.
- Horton, S. (2012). Disposal of Hydrofracking Waste Fluid by Injection into Subsurface Aquifers Triggers Earthquake Swarm in Central Arkansas with Potential for Damaging Earthquake. *Seismological Research Letters*, 83(2), 250–260. doi: 10.1785/gssrl.83.2.250
- Kassambara, A. (2018). ggpubr: ‘ggplot2’ Based Publication Ready Plots. R Package.
- Keranen, K. M., Weingarten, M., Abers, G. A., Bekins, B. A., & Ge, S. (2014). Sharp increase in central Oklahoma seismicity since 2008 induced by massive wastewater injection. *Science*, 345(6195), 448–451. doi: 10.1126/science.1255802

- Khademian, Z., Nakagawa, M., & Ozbay, U. (2018). Modeling injection-induced seismicity through calculation of radiated seismic energy. *Journal of Natural Gas Science and Engineering*, 52(November 2017), 582–590. <https://doi.org/10.1016/j.jngse.2018.02.013>
- King, V. M., Block, L. V., Yeck, W. L., Wood, C. K., & Derouin, S. A. (2014). Geological structure of the Paradox Valley Region, Colorado, and relationship to seismicity induced by deep well injection. *Journal of Geophysical Research: Solid Earth*, 119, 4955–4978.
- Kroll, K. A., Cochran, E. S., & Murray, K. E. (2017, jul). Poroelastic Properties of the Arbuckle Group in Oklahoma Derived from Well Fluid Level Response to the 3 September 2016 M w 5.8 Pawnee and 7 November 2016 M w 5.0 Cushing Earthquakes. *Seismological Research Letters*, 88(4), 963–970. doi: 10.1785/0220160228
- Langenbruch, C., Weingarten, M., & Zoback, M. D. (2018). Physics-based forecasting of man-made earthquake hazards in Oklahoma and Kansas. *Nature Communications*, 9(1), 1–10. doi: 10.1038/s41467-018-06167-4
- Langenbruch, C., Zoback, & D., M. (2016). How will induced seismicity in Oklahoma respond to decreased saltwater injection rates? *Science Advances*, 2(11), 1–10. doi: 10.1126/sciadv.1601542
- Maghsoudi, S., Bar’o, J., Kent, A., Eaton, D., & Davidsen, J. (2018). Interevent triggering in microseismicity induced by hydraulic fracturing. *Bulletin of the Seismological Society of America*, 108(3). doi: 10.1785/0120170368
- Magoon, L. B., & Dow, W. G. (1995). Beyond the petroleum system. *American Association of Petroleum Geologists Bulletin*, 79(12), 1731–1736. doi: 10.1002/2014TC003574.
- McClure, M., Gibson, R., Chiu, K. K., & Ranganath, R. (2017). Identifying potentially induced seismicity and assessing statistical significance in Oklahoma and California. *Journal of Geophysical Research: Solid Earth*, 122(3), 2153–2172. doi: 10.1002/2016JB013711
- McGarr, A. (2014). Maximum magnitude earthquakes induced by fluid injection. *Journal of Geophysical Research: Solid Earth*, 119(2), 1008–1019. doi: 10.1002/2013JB010597
- McGarr, A., Simpson, D., & Seeber, L. (2002). 40 Case histories of induced and triggered seismicity. *International Geophysics*, 81(PART A), 647–661. doi: 10.1016/S0074-6142(02)80243-1
- Mcnamara, D. E., Hayes, G. P., Benz, H. M., Williams, R. A., McMahon, N. D., Aster, R. C., ... Earle, P. (2015). Reactivated faulting near Cushing, Oklahoma: Increased potential for a triggered earthquake in an area of United States strategic infrastructure. *Geophysical Research Letters*, 42, 8328–8332. doi: 10.1002/2015GL064669
- Nolte, K. A., Tsoflias, G. P., Bidgoli, T. S., & Watney, W. L. (2017). Shear-wave anisotropy reveals pore fluid pressure-induced seismicity in the U.S. midcontinent. *Science Advances*, 3(12), 1–6. doi: 10.1126/sciadv.1700443
- Norbeck, J. H., & Rubinstein, J. L. (2018, apr). Hydromechanical Earthquake Nucleation Model Forecasts Onset, Peak, and Falling Rates of Induced Seismicity in Oklahoma and Kansas. *Geophysical Research Letters*, 45(7), 2963–2975. doi: 10.1002/2017GL076562
- OCC. (2017). *Earthquake Response Summary Recent Actions* (Tech. Rep.).

- Ogwari, P. O., Deshon, H. R., & Hornbach, M. J. (2018). The Dallas-Fort Worth Airport Earthquake Sequence: Seismicity Beyond Injection Period. *Journal of Geophysical Research: Solid Earth*, 123, 553–563. doi: 10.1002/2013JB010512
- Peterie, S. L., Miller, R. D., Intfen, J. W., & Gonzales, J. B. (2018). Earthquakes in Kansas Induced by Extremely Far-Field Pressure Diffusion. *Geophysical Research Letters*, 45(3), 1395–1401. doi: 10.1002/2017GL076334
- Petersen, M. D., Mueller, C. S., Moschetti, M. P., Hoover, S. M., Rukstales, K. S., McNamara, D. E., ... Cochran, E. S. (2018). 2018 OneYear Seismic Hazard Forecast for the Central and Eastern United States from Induced and Natural Earthquakes. *Seismological Research Letters*, 89(3), 1049–1061. doi: 10.1785/0220180005
- Pollyea, R. M., Mohammadi, N., Taylor, J. E., & Chapman, M. C. (2018). Geospatial analysis of Oklahoma (USA) earthquakes (20112016): Quantifying the limits of regional-scale earthquake mitigation measures. *Geology*, 46(3), 215–218. doi: 10.1130/G39945.1
- Reasenber, P. (1985, jun). Second-order moment of central California seismicity, 1969–1982. *Journal of Geophysical Research: Solid Earth*, 90(B7), 5479–5495. doi: 10.1029/JB090iB07p05479
- Rubinstein, J. L., Ellsworth, W. L., & Dougherty, S. L. (2018). The 20132016 induced earthquakes in harper and sumner counties, Southern Kansas. *Bulletin of the Seismological Society of America*, 108(2), 674–689. doi: 10.1785/0120170209
- Schoenball, M., Walsh, F. R., Weingarten, M., & Ellsworth, W. L. (2018). How faults wake up: The Guthrie-Langston, Oklahoma earthquakes. *The Leading Edge*, 37(2), 100–106. doi: 10.1190/tle37020100.1
- Schwab, D. R., Bidgoli, T. S., & Taylor, M. H. (2017). Characterizing the Potential for Injection-Induced Fault Reactivation Through Subsurface Structural Mapping and Stress Field Analysis, Wellington Field, Sumner County, Kansas. *Journal of Geophysical Research: Solid Earth*, 122(12), 10,132–10,154. doi: 10.1002/2017JB014071
- Scott Emler, J., Feist Albrecht, S., & Apple, P. (2016). *Second Order Reducing Saltwater Injection Rates* (Tech. Rep.).
- Segall, P., & Lu, S. (2015). Journal of Geophysical Research: Solid Earth Injectioninduced seismicity: Poroelastic and earthquake nucleation effects. 5082–5103. doi: 10.1002/2015JB012060
- Shapiro, S. A. (2015). *Fluid-induced seismicity*. doi: 10.1017/CBO9781139051132
- Sheather, S. J. (2004). Density Estimation. *Statistical Science*. doi: 10.1214/088342304000000297
- Suckale, J. (2010). Moderate-to-large seismicity induced by hydrocarbon production. *The Leading Edge*, 310–319.
- Sumy, D. F., Cochran, E. S., Keranen, K. M., Wei, M., & Abers, G. A. (2014). Observations of static Coulomb stress triggering of the November 2011 M5.7 Oklahoma earthquake sequence. *Journal of Geophysical Research: Solid Earth*, 119, 1904–1923. doi: 10.1002/2013JB010612
- USGS. (2018). *ANSS Comprehensive Earthquake Catalog (ComCat) Documentation*.

- Van Eck, T., Goutbeek, F., Haak, H., & Dost, B. (2006, sep). Seismic hazard due to small-magnitude, shallow-source, induced earthquakes in The Netherlands. *Engineering Geology*, 87(1-2), 105–121. doi: 10.1016/J.ENGGEOL.2006.06.005
- Walsh, F. R., & Zoback, M. D. (2015). Oklahoma’s recent earthquakes and saltwater disposal. *Science Advances*, 1(5), 1–10. doi: 10.1126/sciadv.1500195
- Walsh, F. R., & Zoback, M. D. (2016). Probabilistic assessment of potential fault slip related to injection-induced earthquakes: Application to north-central Oklahoma, USA. *Geology*, 44(12), 991–994. doi: 10.1130/G38275.1
- Weingarten, M., Ge, S., Godt, J. W., Bekins, B. A., & Rubinstein, J. L. (2015). High-rate injection is associated with the increase in U.S. mid-continent seismicity. *Science*, 348(6241), 1336–1340. doi: 10.1126/science.aab1345
- Yeck, W. L., Weingarten, M., Mcnamara, D., & Bergman, E. A. (2016). Far-field pressurization likely caused one of the largest injection induced earthquakes by reactivating a large preexisting basement fault structure. *Geophysical Research Letters* (October), 198–207. doi: 10.1002/2016GL070861
- Zhang, Y., Person, M., Rupp, J., Ellett, K., Celia, M. A., Gable, C. W., Elliot, T. (2013). Hydrogeologic controls on induced seismicity in crystalline basement rocks due to fluid injection into basal reservoirs. *Groundwater*, 51(4), 525–538. doi: 10.1111/gwat.12071

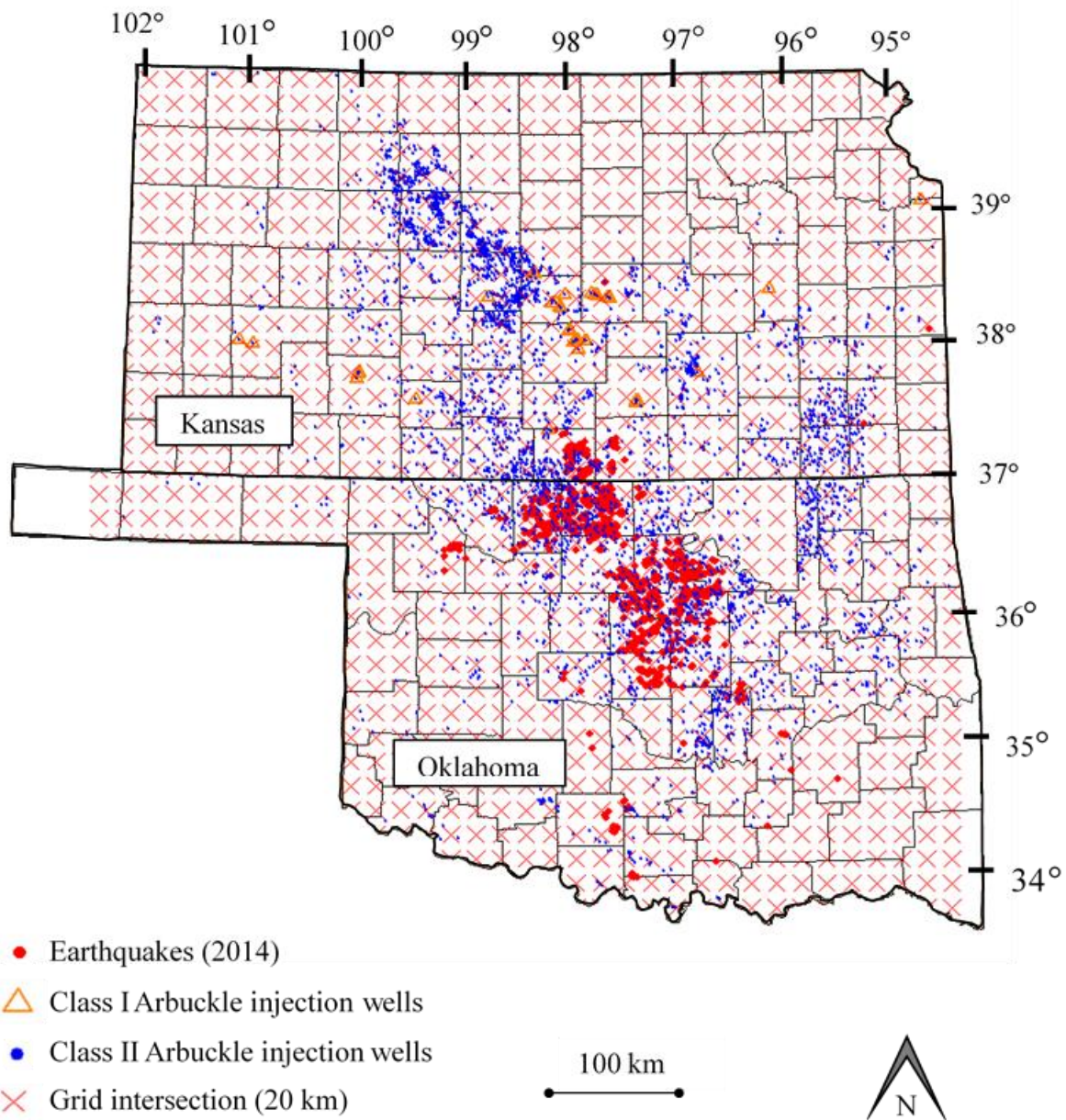


Figure 1: Study map

Map of Kansas and Oklahoma counties showing the locations of Class I (triangles) and II (blue circles) injection wells, as well as 2014 earthquakes (red circles). Intersections for the 20 km bandwidth grid used in the Kernel Density Estimation method are also shown.

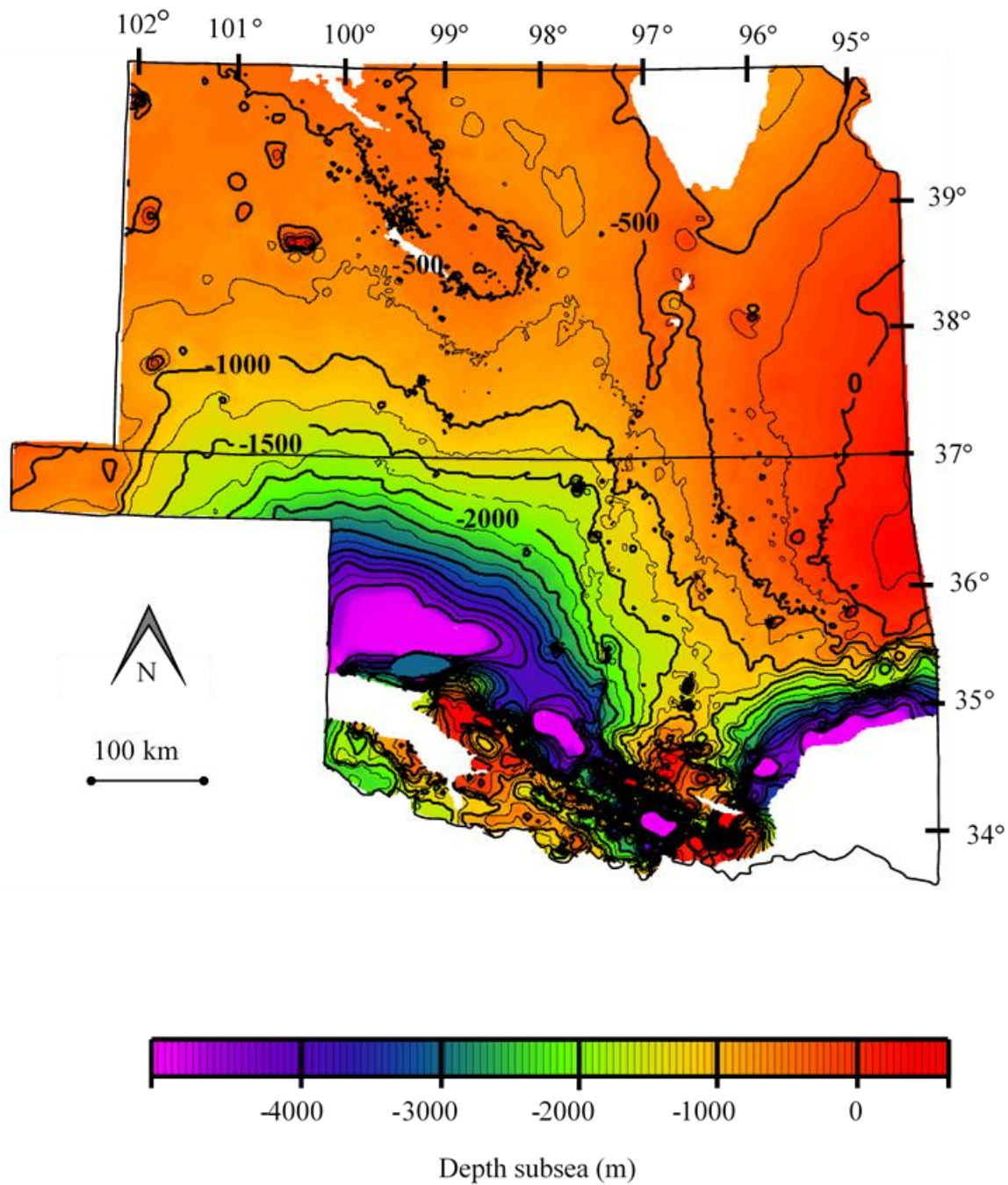


Figure 2: Top-of-Arbuckle Group structure contour map

The top-of-Arbuckle Group interpolated and contoured from stratigraphic picks in 65,879 wells and used to confirm well penetration into the Arbuckle at wells where the disposal interval is not known. The white regions are digitized from Merriam, 1963, to approximate where the Arbuckle is known to be absent.

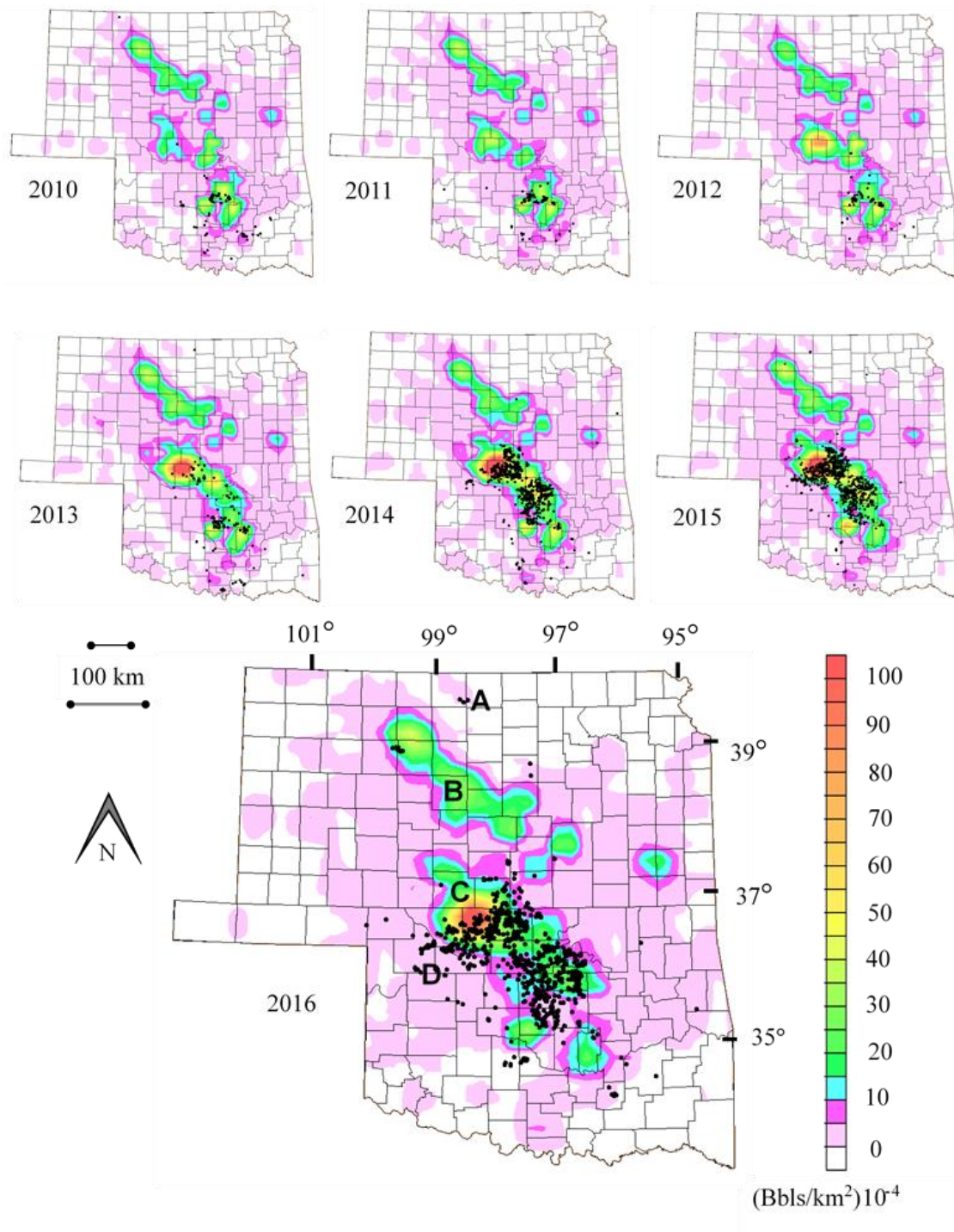


Figure 3: Spatially-averaged surface density of the injected volume

The spatially-averaged injection volume is calculated for each year using the KDE method at a 20 km bandwidth (grid in Figure 1). Earthquakes occurring within the same year are superimposed as black dots. Labels A, B, C, and D identified on year 2016 are areas where the spatiotemporal correlation between injection volume and earthquake frequency is weak or absent.

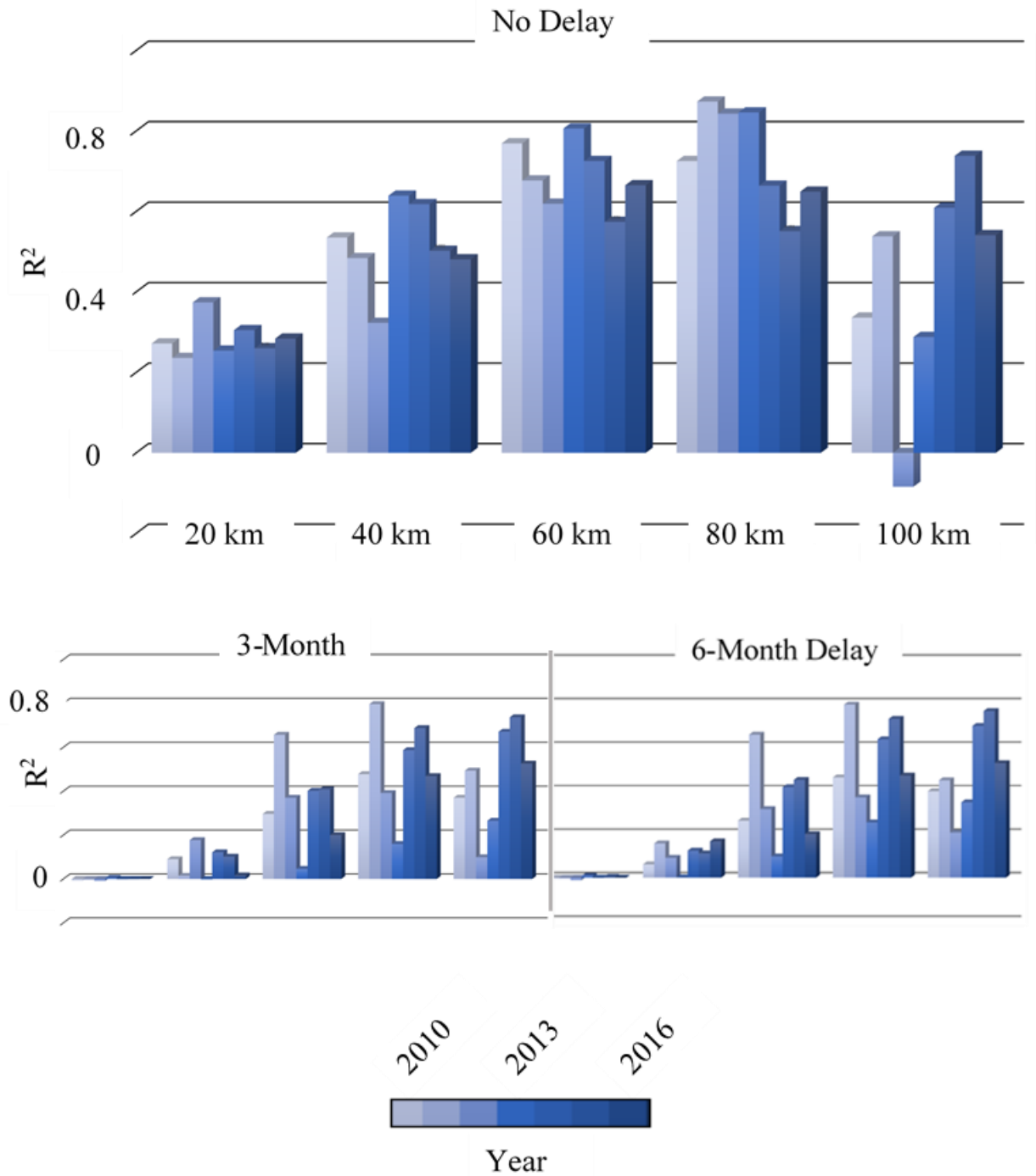


Figure 4: Spatio-temporal linearity of induced seismicity

The linearity of earthquake frequency as a function of injection volume for each year from 2010 through 2017, at various spatial bandwidths. Delaying the earthquakes behind injection volumes (staggered) leads to decrease of linearity.

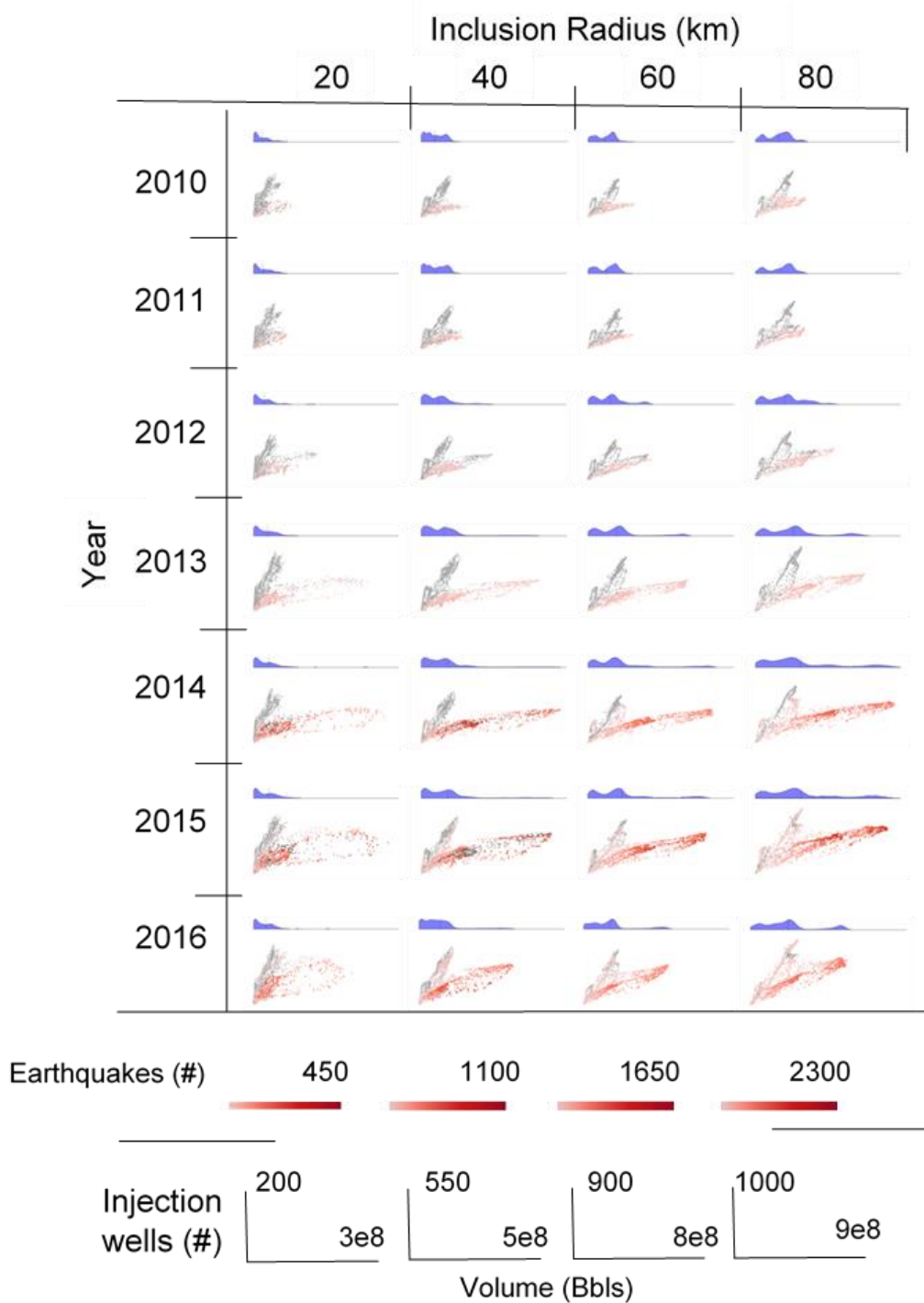


Figure 5: Spatially tracking injected volumes, well-count, and seismicity over time

Each point represents the inclusion radius around a specific injection well. The points are plotted according to the total injection volume (x-axis) and the number of injection wells (y-axis). Kernel density of the volume is provided in blue above each plot. Injection volume increases from 2011 to 2013, preceding seismicity in 2014.

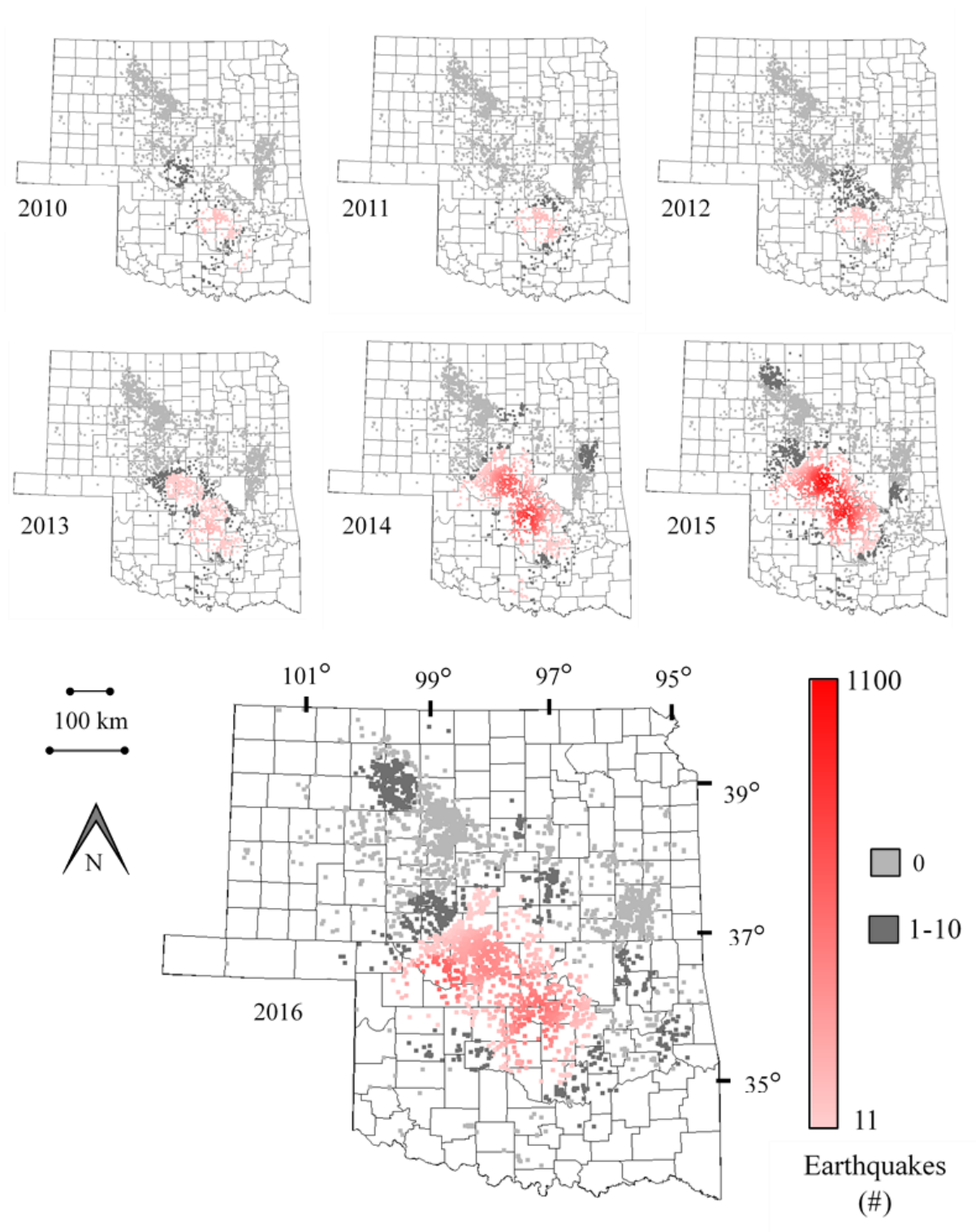


Figure 6: Earthquakes occurring within 40 km of each injection 2010 through 2016

The well locations correspond to the points on Figure 5 and are colored according to the number of earthquakes occurring within a 40 km radius of each well location for each year.

Appendix: Development of cellular petrophysical models of the Arbuckle Group in south-central Kansas

Abstract

In Kansas and Oklahoma, waste-water injection-induced seismicity remains a concern after mitigation efforts and more than a decade of research. An increase in the volume of fluid injected into the Arbuckle Group aquifer has led to pore pressure diffusion and an adjustment of the stress state near critically-stressed faults in the Precambrian crystalline basement. The Arbuckle Group is the primary disposal zone for Oklahoma and Kansas and is a primary oil producing reservoir in Kansas, but has poorly constrained petrophysical properties. The goal of this study is to deduce rock properties by simulating fluid injection and history-matching the results to (1) Arbuckle reservoir pressure measurements and (2) elevated pressures at the depths of earthquake hypocenters. A high resolution geologic structural model was developed across a 17,834 km² area of southern Kansas, using data from 29,601 Kansas oil, gas, and wastewater disposal wells. Wireline logs from over 1,000 wells are used to correlate formation tops and define the model's stratigraphic layering, geometries, and overall architecture. Several 3D cellular models are developed with porosity and permeability leveraged from Arbuckle core analysis, drill-stem tests, and 50+ Arbuckle penetrating wire-line logs.

Introduction

Earthquakes in Kansas and Oklahoma occurred infrequently prior to 2009 (Ellsworth, 2013; Weingarten et al., 2015; Foulger et al., 2018). The onset of seismicity coincides spatially and temporally with development of unconventional oil and gas resources in northern Oklahoma and south-central Kansas. These water-rich reserves occur in Mississippian-aged rock (Evans & Newell, 2013; Choy et al., 2016; Ansari et al., 2019). Water, co-produced with the oil, is disposed into the deeper, Cambro-Ordovician-aged Arbuckle Group (Peterie et al., 2018; Ansari et al., 2019). The Arbuckle Group (hereafter Arbuckle) is the primary oil-producing formation and also serves as the primary target for disposal of unwanted fluid waste (Carr et al., 1986; Franseen et al., 2004; Hearn et al., 2018). Additionally, the Arbuckle is being considered as a potential sink for the long term storage of CO₂ (Benson & Cole, 2008; Scheffer, 2012; Zoback & Gorelick, 2012). The Arbuckle is the lower-most sedimentary formation in the mid-continent's Anadarko Basin and very few wells fully penetrate the formation (Fritz et al., 2012; Keranen et al., 2013). The Arbuckle's structure, porosity, and permeability is poorly understood due to data scarcity and complex reservoir heterogeneity the result of carbonate stratigraphy, paleokarst, diagenesis, and a significant fracture overprint (Carr et al., 1986; Franseen et al., 2004; Fritz et al., 2012).

The need to better understand the Arbuckle aquifer's characteristics has intensified with the sudden onset and rapid increase of seismicity in the mid-continent since 2009. This seismicity has been linked to pore-pressure increases associated with increased volume of fluid-waste injection to the Arbuckle (Ellsworth, 2013; Keranen et al., 2014). First order controls for seismicity are related to geologic structure and the location of critically-stressed faults in the Basement (Ellsworth, 2013; McNamara et al., 2015; Yeck et al., 2016, 2017). The leading physical hypothesis for injection-induced seismicity is that pore pressure perturbations near/at these critically stressed faults cause a shift of the Mohr-Coloumb-failure criterion triggering slip (Ellsworth, 2013; Walsh & Zoback, 2016; X. Zhang et al., 2016; Jin & Zoback, 2018; Schwab et al., 2017). The seismicity, pore-pressure perturbations, and the observed increases of Arbuckle reservoir pressure and static-fluid-level measurements are the result of injection into the Arbuckle (Langenbruch et al., 2018; Norbeck & Rubinstein, 2018; Peterie et al., 2018; Ansari et al., 2019).

A decade of midcontinent induced-seismicity has resulted in numerous efforts to record, catalog, and make available data that is useful for investigators. Research has resulted in physical models (Choy et al., 2016; X. Zhang et al., 2016; Langenbruch et al., 2018; Norbeck & Rubinstein, 2018), stress-state models (Alt & Zoback, 2017; Barbour et al., 2017; Schwab et al., 2017; Nolte et al., 2017; Jin & Zoback, 2018; Hearn et al., 2018), numeric models (X. Zhang et al., 2016; Hearn et al., 2018), statistical models (McClure et al., 2017; Pollyea et al., 2018; Peterie et al., 2018; Ansari et al., 2019), and risk assessment models (Langenbruch et al., 2018).

Recent studies show that increases of Arbuckle fluid disposal has led to pressure increases in (1) the Arbuckle aquifer (Peterie et al., 2018; Ansari et al., 2019) and (2) the basement (Y. Zhang et al., 2013; Yeck et al., 2016; Langenbruch et al., 2018). This study posits that the rock properties must then be capable of honoring the dynamic pressure measurements observed in the Arbuckle and also elevate pressures at the time and location of earthquake hypocenters. This goal is to deduce rock properties in the Arbuckle, by simulating pressure responses to injection in a high-resolution model, and comparing the simulated results to real-world pressure measurements. A successfully history-matched Arbuckle model is used in combined with an isotropic basement model, to investigate basement properties by using simulation-based optimization.

Background

Injection into the Arbuckle is historically favorable due to its separation from potable water resources, and because fluid can be gravity-fed into the under-pressurized aquifer (Carr et al., 1986; Franseen et al., 2004). Reservoir pressures and static-water levels are increasing as a result of injection into a finite saline aquifer (Peterie et al., 2018; Ansari et al., 2019). Injection induced seismicity has resulted in state-mandated volume restrictions the plugging-back of specific, deep and high-rate injection wells (Baker, 2016; Scott Emler et al., 2016; OCC, 2017), but the issue remains a concern (Keranen & Weingarten, 2018; Peterie et al., 2018; Ansari et al., 2019).

Modeling the Arbuckle petrophysical properties has difficulties that are exacerbated by the scarcity of data. The Arbuckle is the deepest sedimentary formation and there is limited economic reason for conducting expensive drilling and testing beyond the operational necessity. Few well penetrations exceed 60 meters into an Arbuckle that ranges to thicknesses of 420 meters in Kansas (Keroher & Kirby, 1948; Carr et al., 1986; Franseen et al., 2004; Fritz et al., 2012). In special cases where deeper wells do have significant penetration, modeling permeability based upon logs or core analyses has had only measured success when considered with respect to operational observations (e.g. pumping rates) and hydraulic testing (Carr et al., 1986). The discrepancy, and a primary reason for why modeling the Arbuckle has proven difficult, is due to the scale-dependent properties of permeability and the indirect methods of calculating it (Doveton, 2014). The layered carbonate stratigraphy of the Arbuckle, combined with repeated diagenetic alterations and a fracture overprint, limits our ability to up-scale discrete measurements from log or core. The complexities also make delineating flow-units (petrofacies) extremely difficult, albeit necessary in order to achieve an accurate history match (Carr et al., 1986; W. L. Watney et al., 1998; Doveton, 2014).

The Wellington oil field in Sumner County, Kansas, was recently studied closely for the purpose of identifying storage potential of the Arbuckle (Scheffer, 2012; Holubnyak et al., 2013). Among many of the important conclusions drawn from investigation at the Wellington Field, Scheffer concludes there is strong evidence of hydraulic separation between the upper and lower Arbuckle (Scheffer, 2012). The suspected baffle is interpreted primarily by 1) nuclear magnetic resonance (NMR) wireline log analysis, 2) core description, 3) 3D seismic data, and 4) geochemistry of fluid brines (Scheffer, 2012). Permeability was calculated from NMR log via the Timur-Coates transform, resulting in a wide range of permeability throughout the Arbuckle at the log-scale from .001 mD to nearly 1000 mD.

Overall, the NMR calculated permeability is relatively lower in the middle of the Arbuckle (Scheffer, 2012; Holubnyak et al., 2013; W. L. Watney et al., 2014). The middle portion of the Arbuckle core (70m to 180m) is described as dominantly tight, dense, micritic dolomite, with occasional inter-crystalline porosity (Scheffer, 2012; Holubnyak et al., 2013; W. L. Watney et al., 2014). Vertical fractures are common throughout the core but are bedding constrained (Scheffer, 2012). Seismic data of the Wellington Field indicates that this middle section of the Arbuckle has a relatively lower impedance, interpreted as reflective of a relatively higher rock density and in support of the hypothesis that there is a middle-Arbuckle hydraulic barrier (Scheffer, 2012; Holubnyak et al., 2013; W. L. Watney et al., 2014). Note, faulting is seen offsetting pre-Pennsylvanian aged rock (Mississippi, Arbuckle, and basement) in the same seismic volume (Schwab et al., 2017). Fluid brine data was over-saturated with respect to aragonite and calcite, becoming less saturated with depth (Scheffer, 2012). Although the fluid brine data clusters suggest different geochemistry above and below the baffle, Scheffer notes the linearity of the geochemical data, and several potential controls that could account for the measurements, including mixture and diffusion throughout a hydraulically connected Arbuckle.

Numerical groundwater flow modeling near the Wellington Field was recently conducted to assess hydraulic properties of high-rate injection and the nearby induced slip of the Milan earthquake, a 4.8 magnitude event that occurred approximately 20 km west of the Wellington Field on November 12, 2014 (Hearn et al., 2018). The Hearn Arbuckle model contains a lower hydraulic conductivity zone in the middle to reflect the observations by Scheffer at the Wellington Field. The layers are modeled with hydraulic conductivity defined in the upper, middle, and lower zone as 0.25 m/d, 0.00008 m/d, and 0.25 m/d, respectively. Hearn notes that it is imperative to discern whether the middle Arbuckle does act as a baffle because of the large number of low volume Arbuckle Injection Wells which inject into only the upper portion of the Arbuckle (Hearn et al., 2018).

This study seeks to overcome these challenges by developing a model in an area rich with static and dynamic data. Publicly available data is used for model development, simulation, and history-matching with the goal of deducing porosity and permeability in the Arbuckle and basement at the scale of induced seismicity.

Data

The study area and geologic model covers a 13,230 km² area in the south-central part of the state, encompassing Kingman, Sedgwick, Harper, and Sumner counties, as presented on Figures 1 and 2. Data incorporated into the model come from four sources, described below and presented in Figure 1.

The Kansas Geological Survey (KGS) library, which maintains records of well information (well locations, well logs, formation tops, and well test results). The model area contains 29,601 wells (Figure 2), 17,834 km² wells with recorded Mississippian stratigraphic tops or picks (Figure 3), 2110 wells with a recorded Arbuckle tops (Figure 4), 49 wire-line porosity logs that penetrate the Arbuckle greater than 60 m, and 2 study wells with drill-stem-tests and core at various intervals within the Arbuckle. Spurious data points were identified and corrected on a well-to-well basis (e.g.

multiple but different entries on the same well or different nomenclature for the same formation top). The Kansas Corporation Commission requires that operators of Class II disposal wells (injection of waste-fluid co-produced with the production of oil) report annual cumulative injection volumes. The KGS provides these historic injection records to the public via their website (Kansas Geological Survey, n.d.). There are 319 Arbuckle injection wells in the model area with associated injection volumes (Figures 1 and 5) recorded as a single cumulative total volume for each year 2010 through 2016.

The Kansas Department of Health and Environment requires operators to perform well and reservoir tests for Class I disposal wells (disposal of hazardous and nonhazardous fluid waste, typically from industrial facilities) which includes reservoir pressure fall-off tests in addition to tracking and reporting of the disposal volumes. There are two Class I disposal wells in the Model area (Figure 1).

The United States Geological Survey (USGS) ANSS Comprehensive Earthquake Catalog (ComCat) is available to the public via their website (USGS, 2018). There are 450 earthquakes in the model area, occurring from 2013 (first occurrence) through 2017, with a magnitude 2.5 or greater (Figures 1 and 5).

Injection volumes data was filtered to include only Arbuckle and deeper wells. The Arbuckle is assumed to be in hydraulic communication with the basement. Injection into shallower zones, particularly zones shallower than the Mississippian, are likely to be hydraulically separated from deep faults in the basement by low-permeable seals. All data were collated and standardized to the NAD-27 projection for southern Kansas.

Methods

The following subsections describe the methods as they pertain to high-resolution structure modeling and petrophysical modeling. The order is reflective of work-flow, which followed standard procedures for developing a 3D cellular model in Schlumberger's Petrel™ modeling software. The 3D cellular wire-frame of the Arbuckle was developed by correlating stratigraphy across more than 1074 wire-line logs and creating grids that honor a tops database of 29,601 oil and gas wells. A petrophysical analysis of porosity and permeability is up-scaled into the model from wire-line logs, core, and drill-stem tests. Injection wells are incorporated in the model and their associated record of annual injection volumes is used as the simulation input.

First, a high-resolution 3D cellular model of the Arbuckle is developed. Second, reservoir characteristics are leveraged from log analysis, core, and drill-stem-test, before being up-scaled and modeled for simulation. Third, the models are used to simulate pressure-response (output) to fluid injection (input). The simulated results are compared to Class I Arbuckle pressure data.

High-resolution structure modeling

A 2D regular Cartesian grid was constructed in alignment with cardinal directions and with increments of 1200 feet (365.7 m). The resulting plane has 133,308 facets from 322 rows and 414 columns. All of the stratigraphic horizons and isopach grids used in the model have these

dimensions, so that grid-to-grid operations could be easily performed (e.g. subtracting an isopach from a horizon to produce a deeper horizon).

Mississippian-aged strata are primary targets for oil production in the area and the most commonly recorded formation top in the KGS database is the top of the Mississippian (Pennsylvanian-Mississippian unconformity). A top Mississippian grid was modeled according to 13,226 Mississippian entries using Minimum Curvature interpolation and Grid-Flexure algorithms (IHS-PetraTM). The top of the Arbuckle was modeled in the same manner, but with 2110 data entries (Figure 4). Of the 2110 stratigraphic entries for the Arbuckle, 319 are active injection wells with corresponding injection volume data.

The Arbuckle model has 12 layers developed from well-to-well wireline log correlation. Horizons were established by correlating high-gamma ray readings in wireline logs that may correspond to laterally-continuous shales. Thin layers were also recognized and correlated using the neutron porosity logs. These layers were identified from spikes in the neutron porosity measurements that were otherwise flat-reading through the Arbuckle. The horizons stack to form the model layering. The layers are connected via vertical pillars located at grid-intersections to form a layered 3D wire-frame.

Interval thicknesses was calculated at each well and modeled to grids using minimum curvature interpolation. Grid-to-grid operations were performed in order to retain the higher resolution structure of the top of the Arbuckle. The upper-most Arbuckle isopach was subtracted from the top-of-Arbuckle grid and a layered model was thereby constructed by subtracting each individual isopach grid from the above gridded horizon, advancing downward from the top of-Arbuckle to the basement. In a general sense, the structural differences between each layer is insignificant, simply copies of the top-of-Arbuckle grid translated downward and tweaked to honor the correlations. Geometric statistics of the static 3D cellular model and layering are presented on Table 1.

Petrophysical Property Modeling

The 3D wireframe model was populated with log porosity, log permeability, core porosity, core permeability, and drill-stem-test permeability. The raw measurements of porosity and permeability are statistically up-scaled first, to the well-scale (log format); second, into the cells intersected by the well-path; and third, into the adjacent layering. The process resulted in two porosity models (log and core) and three permeability models (log, core, and drill-stem-test).

Log Porosity

Porosity (φ) was calculated at 49 wells by averaging neutron porosity (n_φ) and density porosity (d_φ) into a single log with a single percentage volume porosity for each 0.5 ft-increment, following:

$$(n_\varphi + d_\varphi)/2 = \varphi$$

These logs were then arithmetically up-scaled to cells penetrated by the well-path. The populated cell-values (at the well-path) were then modeled into adjacent layering to develop 5 realizations using random-Gaussian simulation.

Log Permeability

Of the logs with significant Arbuckle penetration in the KGS database, 9 included a permeability log. Each was evaluated separately and all appear to have been calculated using proprietary techniques which take advantage of a particular suite of logs. In the case of the Wellington KGS-32 study well the permeability log was calculated using NMR (Scheffer, 2012). The logs were harmonically up-scaled to the cells which are penetrated by the well-path. These cell-values were then modeled into adjacent layering to develop 5 realizations using random-Gaussian simulation.

Core Porosity

The porosity is presented in core-analysis reports as a single percentage occurring over a discrete thickness (the section of core tested). These values were placed directly into a pseudo-log, un-averaged. The log-interval is not standard (for example one measurement at each 0.5 foot increment) but instead is fixed to the reported discrete thickness. The log has gaps where porosity was not measured, or core was not retrieved, and in these instances the log is made to be empty (null as opposed to zero). The pseudo-log was up-scaled numerically into cells penetrated by the well-path. These cell-values were then modeled into the adjacent layering to develop 5 realizations with random-Gaussian simulation.

Core Permeability

Up-scaling core permeability from 4 wells with core-analysis reports followed the same procedure as core porosity (direct placement into a pseudo-log). In the case of permeability, however, the pseudo-log was up-scaled harmonically to cells penetrated by the well-path. These cell-values were then modeled into the adjacent layering to develop 5 realizations with random-Gaussian simulation.

Drill-stem-test Permeability

Permeability was leveraged from drill-stem-test by making use of the Horner Plot (Horner, 1951; Maier, 1962) and the following relationships (The Kansas Geological Survey, n.d.).

$$P = P_f - m(\log_{10})[(T + dT)/dT]$$

P = pressure

P_f = formation pressure
m = pressure/cycle

T = Temperature

$$K(h/\mu) = 162.6(B/m)q$$

q = flow rate

μ = viscosity

B = formation volume factor

h = vertical thickness of test

K = average effective permeability

Flow rate is extrapolated from the volume of fluid extracted during the test and the test duration.

Increasing viscosity of the fluid in the drill-stem-test leads to increased permeability calculations (all other variables held constant). Ideally, the viscosity should be reflective of the fluid actually used in the drill-stem-testing. In the process of drilling, drilling mud (bentonite) is used to prevent cave-in. Management of the drilling mud rheological properties is essential to a successful drilling operation and a mud-manager will commonly make use of a Marsh funnel to get a field-measurement of the drilling-mud viscosity (Marsh, 1931; Doveton, 2014; Elkatatny, 2016).

The DST-based model is the result of calculating viscosity based on Marsh funnel measurements recorded for each drill-stem-tested interval on the DST report. In the Marsh funnel test, extracted fluid is poured through a "Marsh" funnel, and the time (seconds) for 1-quart of fluid to drain from the funnel is documented on the test report (Marsh, 1931; Pitt, 2000; Almahdawi et al., 2014; Kamenar et al., n.d.; Elkatatny, 2016). There are many methods for calculating apparent viscosity, and other rheological fluid properties, from the Marsh test, which are ultimately relationships between the volume (1-quart), time (seconds to drain), and funnel specifications (cone-shaped) (Pitt, 2000; Almahdawi et al., 2014; Elkatatny, 2016). Viscosity was calculated from Marsh test measurements (recorded on the DST reports) using the simplified equation in the manner of Pitt (Pitt, 2000).

$$\mu = \rho(t - 25)$$

t = drainage time (seconds)

ρ = fluid density (g/cm^3)

μ = viscosity (cP)

The drill-stem-test is also performed over a discrete interval (by setting a packer below and above the test-interval). Calculating permeability requires an interval thickness. Scheffer calculated viscosity from drill-stem-test of the KGS-Wellington 32 well, and used an 8[%] porosity cut-off (Scheffer, 2012). In this study, the entire interval of the test was used to calculate permeability.

The resulting permeability was placed into a pseudo-log format, in the same manner as Core porosity and permeability. There is one value per log-interval the size of the test interval. The permeability was then arithmetically up-scaled to the cells penetrated by the well path and modeled into adjacent layering five times (realizations) using random-Gaussian simulation.

Results

Structural Results

The top-of-Mississippi and top-of-Arbuckle grids were contoured and are presented as Figures 3 and 4. The isopach that results from subtracting the Mississippian Grid from the Arbuckle Grid is also contoured and presented as Figure 6.

The Arbuckle model consists of 1,413,571 cells subdivided into 12 unique layers. The model is 117.7 km long in the i-direction (north-south), 151.4km in the j-direction (east-west) and ranges in thickness from 245m to 365m and depths from -1139.38 to -4363.90 ft-subsea. The structural character of individual layers are presented on Table 1.

Petrophysical Results

There are five petrophysical property realizations produced, using random Gaussian simulation, for each data-source (wireline log porosity, wireline log permeability, core porosity, core permeability, and drill-stem test). The result is 15 permeability models (3 methods x 5 realizations) and 10 porosity models (2 methods x 5 realizations) which can be combined for 150 unique simulation-ready models.

In general, the realizations are statistically similar when up-scaled from the same source of data. Up-scaled from wireline log layer-porosity ranges from 0.4 to 16.4 percent with an overall mean around 5 percent. Permeability up-scaled from wireline log calculations ranges from 0.1 to 6.1 millidarcy with an overall mean around 0.8 millidarcy. Up-scaled core-analysis measurements of porosity range from 0.4 to 16.4 percent with an overall mean around 4 percent. Permeability up-scaled from core analysis ranges from 0.01 to 33.6 millidarcy with an overall mean of around 4.2 millidarcy. The highest permeability models are up-scaled drill-stem-test calculations of permeability which range from 3.1 millidarcy to 2.6 Darcy with an overall mean of around 1 Darcy. A summary of the porosity/permeability statistics for each layer and model is presented on Tables 2 through 6.

Discussion and Future work

The Arbuckle structure map (Figure 4) is interesting because there are readily identifiable structures despite the very high-resolution and use of Minimum Curvature and grid flexure (which resists changes to the topography). These structures are oriented in rough approximation to the previously recognized faults of the Humboldt fault zone (Merriam, 1963; Schwab et al., 2017). The isopach between the top of Arbuckle and the top of the Mississippian is likewise useful for identifying structures.

The petrophysical models described above will be used in conjunction with dynamic injection, pressure, and seismicity data to drive simulations of injection and constrain reservoir properties through history-matching to pressure-response. A history-matched model can reveal how injection-induced pressure diffusion occurs throughout the Arbuckle to trigger critically stressed faults in the basement. The models are meant to be a 'first-cut' analysis and will need to be refined in order to achieve an accurate history match.

Limitations

The data used for property modeling are grossly abstracted during the upscaling and modeling process required to go from discrete-measurements at the well-scale (or smaller) to the 3D volume of the model layering.

Fluid dynamics are controlled not only by petrographic reservoir properties porosity and permeability, but are also heavily controlled by other variables including fluid properties (compressibility, viscosity, surface tension, vapor pressure, salinity), hydraulic diffusivity, transmissivity, laminar flow and boundary layer flow, pressure distribution, and thermodynamics (Potter & Foss, 1975).

There are problems with Marsh Funnel estimates that solve rheological parameters uniquely and different fluids can have different rheological properties (Balhoff et al., 2011).

Acknowledgments

The supplementary materials contain the Arbuckle injection well location, volume data, and the earthquake locations and times. SuppWe thank G. Bohling, C. Jackson, A. Nolte, G. Tsoflis, R. Mandel, J. Jennings, and E. Holubnyak for their contributions and discussions. We thank the KCC, OCC, KGS, and KDHE for maintaining and helping us access publicly available data. We thank IHS Markit for donating licenses for use of *Petra*TM, Schlumberger for donating licenses for use of *Petrel*TM. This material is based upon work supported by the U.S. Geological Survey under Grant No. G16AP00022 to Bidgoli. The views and conclusions contained in this document are those of the authors and should not be interpreted as representing the opinions of the U.S. Geological Survey. The authors have no interests or affiliations perceived as a conflict of interest with respect to the results of this paper.

References

- Almahdawi, F. H. M., Al-Yaseri, A. Z., & Jasim, N. (2014). Apparent Viscosity Direct from Marsh Funnel Test. *Iraqi Journal of Chemical and Petroleum Engineering*, 15(1), 51–57.
- Alt, R. C., & Zoback, M. D. (2017). In situ stress and active faulting in Oklahoma. *Bulletin of the Seismological Society of America*, 107(1). doi: 10.1785/0120160156
- Ansari, A. E., Bidgoli, T. S., & Hollenbach, A. (2019). Accelerated fill-up of the Arbuckle Group aquifer and links to U.S. midcontinent seismicity. *Journal of Geophysical Research: Solid Earth*, 25. doi: 10.1029/2018JB016926
- Baker, T. (2016). *Media Advisory - Regional Earthquake Response Plan for Central Oklahoma and Expansion of the Area of Interest* (Tech. Rep.). OCC.
- Balhoff, M. T., Lake, L. W., Bommer, P. M., Lewis, R. E., Weber, M. J., & Calderin, J. M. (2011). Rheological and yield stress measurements of non-Newtonian fluids using a Marsh Funnel. *Journal of Petroleum Science and Engineering*, 77, 393–402. doi: 10.1016/j.petrol.2011.04.008
- Barbour, A. J., Norbeck, J. H., & Rubinstein, J. L. (2017). The Effects of Varying Injection Rates in Osage County, Oklahoma, on the 2016 M w 5.8 Pawnee Earthquake. *Seismological Research Letters*, 88(4), 1040–1053. doi: 10.1785/0220170003
- Benson, S. M., & Cole, D. R. (2008). CO 2 Sequestration in Deep Sedimentary Formations. *Geoscience Elements*, 4, 325–331. doi: 10.2113/gselements.4.5.325
- Carr, J. E., McGovern, H. E., Gogel, T., & Doveton, J. H. (1984). *Geohydrology of and potential for fluid disposal in the Arbuckle aquifer in Kansas* (Tech. Rep.). Lawrence, Kansas: U.S. Geological Survey Open-File Report.
- Choy, G. L., Rubinstein, J. L., Yeck, W. L., McNamara, D. E., Mueller, C. S., & Boyd, O. S. (2016). A Rare Moderate Sized M4.9 Earthquake in Kansas: Rupture Process of the Milan, Kansas, Earthquake of 12 November 2014 and Its Relationship to Fluid Injection. *Seismological Research Letters*, 87(6). doi: 10.1785/0220160100
- Doveton, J. (2014). *Principles of Mathematical Petrophysics*.
- Elkhatatny, S. M. (2016). Determination the Rheological Properties of Invert Emulsion Based Mud on Real Time Using Artificial Neural Network. *Society of Petroleum Engineers (SPE-182801-MS)*. doi: 10.2118/182801-ms
- Ellsworth, W. L. (2013). Injection-Induced Earthquakes. *Science*, 341(July), 1–7.
- Evans, C. S., & Newell, K. D. (2013). The Mississippian Limestone Play in Kansas : Oil and Gas in a Complex Geologic Setting. *Kansas Geological Survey Public Information Circular*, 33(March), 1–6.
- Foulger, G. R., Wilson, M. P., Gluyas, J. G., Julian, B. R., & Davies, R. J. (2018). Global review of human-induced earthquakes. *Earth-Science Reviews*, 178. doi: 10.1016/j.earscirev.2017.07.008
- Franseen, E. K., Byrnes, A. P., Cansler, J. R., Steinhauft, D. M., & Carr, T. R. (2004). The Geology of Kansas Historical Aspects of Arbuckle. *Kansas Geological Survey Earth Sciences Bulletin*, 250(part 2), 1–43.
- Fritz, R., Medlock, P., Kuykendall, M. J., & Wilson, J. L. (2012). The Geology of the Arbuckle Group in the Midcontinent: Sequence Stratigraphy, Reservoir Development, and the Potential for Hydrocarbon Exploration. In J. Derby & R. Fritz (Eds.), *The great american carbonate bank: The geology and economic resources of the cambrian - ordovician sauk megasequence of laurentia* (98th ed., pp. 208–273). AAPG Memoir. doi: 10.1306/13331495M980077

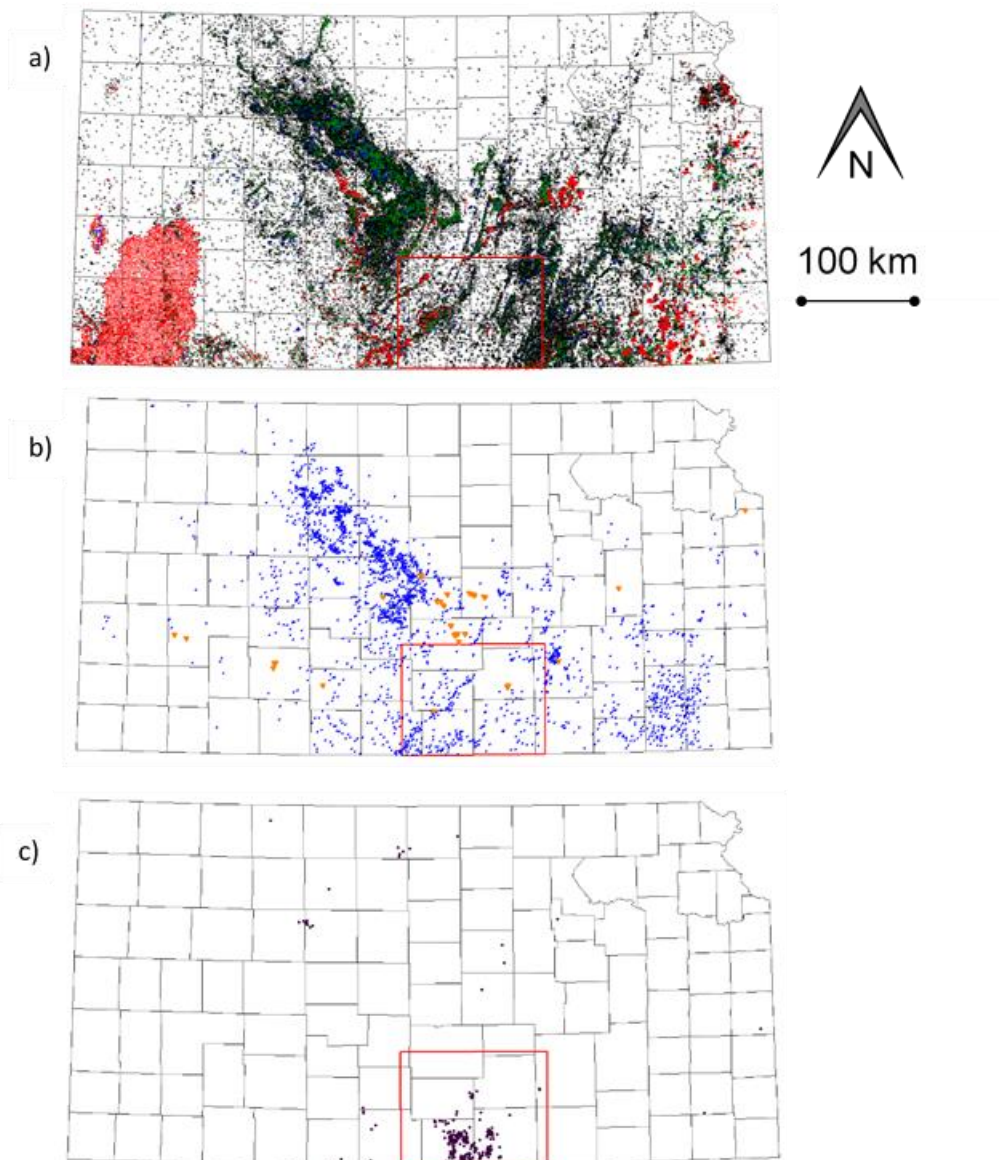
- Hearn, E. H., Koltermann, C., & Rubinstein, J. R. (2018). Numerical Models of Pore Pressure and Stress Changes Along Basement Faults Due to Wastewater Injection: Applications to the 2014 Milan, Kansas Earthquake. *Geochemistry, Geophysics, Geosystems*. doi: 10.1002/2017GC007194
- Holubnyak, Y., Watney, W. L., Rush, J., Birdie, T., Fazelalavi, M., & Raney, J. (2013). Dynamic Simulation of Pilot Scale CO₂ Injection into the Arbuckle Saline Aquifer at Wellington Field in Southern Kansas. In *Agu fall meeting abstracts*.
- Horner, D. R. (1951). Pressure Build-up in Wells. In *3rd world petroleum congress section ii* (pp. 503–521).
- Jin, L., & Zoback, M. D. (2018). Modeling Induced Seismicity : Co-Seismic Fully Dynamic Spontaneous Rupture Considering Fault Poroelastic Stress. In *American rock mechanics association- 52nd us rock mechanics / geomechanics symposium*.
- Kamenar, A., Taco, G., & Edgoose, J.(n.d.). *How to plan a safe and successful permeability test program in coal seams Publication Details* (Tech.Rep.).
- Kansas Geological Survey. (n.d.). *KGS–Energy Resources–Oil and Gas Data Bases*.
- Keranen, K. M., Savage, H. M., Abers, G. A., & Cochran, E. S. (2013). Potentially induced earthquakes in Oklahoma, USA: Links between wastewater injection and the 2011 Mw 5.7 earthquake sequence. *Geology*. doi: 10.1130/G34045.1
- Keranen, K. M., & Weingarten, M. (2018, may). Induced Seismicity. *Annual Review of Earth and Planetary Sciences*, 46(1), 149–174.
- Keranen, K. M., Weingarten, M., Abers, G. A., Bekins, B. A., & Ge, S. (2014). Sharp increase in central Oklahoma seismicity since 2008 induced by massive wastewater injection. *Science*, 345(6195), 448–451. doi: 10.1126/ science.1255802
- Keroher, R. P., & Kirby, J. J. (1948). Upper Cambrian and Lower Ordovician Rocks in Kansas. *Kansas Geological Survey Bulletin*, 72.
- Langenbruch, C., Weingarten, M., & Zoback, M. D. (2018). Physics-based forecasting of man-made earthquake hazards in Oklahoma and Kansas. *Nature Communications*, 9(1), 1–10. doi: 10.1038/s41467-018-06167-4
- Maier, L. (1962). Recent Developments in the Interpretation and Application of DST Data. *SPE Reservoir Evaluation & Engineering Engineering*, 14(11), 1213–1222. doi: 10.2118/290-pa
- Marsh, H. N. (1931). Properties and Treatment of Rotary Mud. *Transactions of the AIME*, 92(01), 234–251.
- McClure, M., Gibson, R., Chiu, K. K., & Ranganath, R. (2017). Identifying potentially induced seismicity and assessing statistical significance in Oklahoma and California. *Journal of Geophysical Research: Solid Earth*, 122(3), 2153–2172. doi: 10.1002/2016JB013711
- McNamara, D. E., Benz, H. M., Herrmann, R. B., Bergman, E. A., Earle, P., Holland, A., ... Gassner, A. (2015). Earthquake hypocenters and focal mechanisms in central Oklahoma reveal a complex system of reactivated subsurface strike-slip faulting. *Geophysical Research Letters*, 42(8), 2742–2749. doi: 10.1002/2014GL062730
- Merriam, D. F. (1963). Geologic History of Kansas. *Kansas Geological Survey Bulletin*, 162.
- Nolte, K. A., Tsoflias, G. P., Bidgoli, T. S., & Watney, W. L. (2017). Shear-wave anisotropy reveals pore fluid pressure-induced seismicity in the U.S. midcontinent. *Science Advances*, 3(12), 1–6. doi: 10.1126/sciadv.1700443

- Norbeck, J. H., & Rubinstein, J. L. (2018, apr). Hydromechanical Earthquake Nucleation Model Forecasts Onset, Peak, and Falling Rates of Induced Seismicity in Oklahoma and Kansas. *Geophysical Research Letters*, 45(7), 2963–2975. doi: 10.1002/2017GL076562
- OCC. (2017). *Earthquake Response Summary Recent Actions* (Tech. Rep.). Retrieved from <http://www.occeweb.com/News/01-04-16EQADVISORY.pdf>
- Peterie, S. L., Miller, R. D., Intfen, J. W., & Gonzales, J. B. (2018). Earthquakes in Kansas Induced by Extremely Far-Field Pressure Diffusion. *Geophysical Research Letters*, 45(3), 1395–1401. doi: 10.1002/2017GL076334
- Pitt, M. (2000). The Marsh Funnel and Drilling Fluid Viscosity: A New Equation for Field Use. *SPE Drilling & Completion*, 15(01), 3–6. doi: 10.2118/62020 -pa
- Pollyea, R. M., Mohammadi, N., Taylor, J. E., & Chapman, M. C. (2018). Geospatial analysis of Oklahoma (USA) earthquakes (20112016): Quantifying the limits of regional-scale earthquake mitigation measures. *Geology*, 46(3), 215–218. doi: 10.1130/G39945.1
- Potter, M. C., & Foss, J. J. (1975). *Fluid Mechanics*. Ronald Press, U.S.
- Scheffer, A. (2012). *Geochemical and Microbiological Characterization of the Arbuckle Saline Aquifer, a Potential CO 2 Storage Reservoir; Implications for Hydraulic Separation and Caprock Integrity* (Unpublished doctoral dissertation). University of Kansas.
- Schwab, D. R., Bidgoli, T. S., & Taylor, M. H. (2017). Characterizing the Potential for Injection-Induced Fault Reactivation Through Subsurface Structural Mapping and Stress Field Analysis, Wellington Field, Sumner County, Kansas. *Journal of Geophysical Research: Solid Earth*, 122(12), 10,132–10,154. doi: 10.1002/2017JB014071
- Scott Emler, J., Feist Albrecht, S., & Apple, P. (2016). *Second Order Reducing Saltwater Injection Rates* (Tech. Rep.).
- The Kansas Geological Survey. (n.d.). *HELP: Quantitative Analysis Equations Fluid DST*. Retrieved 2019-03-06, from http://www.kgs.ku.edu/software/DST/HELP/horner/qa_{ }fluid.html
- USGS. (2018). *ANSS Comprehensive Earthquake Catalog (ComCat) Documentation*. Retrieved 2018-12-15, from <https://earthquake.usgs.gov/data/comcat/>
- Walsh, F. R., & Zoback, M. D. (2016). Probabilistic assessment of potential fault slip related to injection induced earthquakes: Application to north-central Oklahoma, USA. *Geology*, 44(12), 991–994. doi: 10.1130/G38275.1
- Watney, L. W., Rankey, E. C., & Harbaugh, J. (1999). Perspectives on Stratigraphic Simulation Models. *SEPM Special Publication*, 62(62).
- Watney, W. L., Doveton, J. H., Bhattacharya, S., Gerlach, P., Bohling, G. C., & Carr, T. (1998). Petrofacies Analysis - A Petrophysical Tool for Geologic/Engineering Reservoir Characterization. *AAPG Memoir* (71), 73–90.
- Watney, W. L., Ph, D., Birdie, T., & Ph, D. (2014). Geologic Carbon Storage in the Lower Ordovician Arbuckle Group Saline Aquifer in Kansas. In *National groundwater association summit* (p. 21). NGWA.
- Weingarten, M., Ge, S., Godt, J. W., Bekins, B. A., & Rubinstein, J. L. (2015). High-rate injection is associated with the increase in U.S. mid-continent seismicity. *Science*, 348(6241), 1336–1340. doi: 10.1126/science.aab1345

- Yeck, W. L., Hayes, G. P., McNamara, D. E., Rubinstein, J. L., Barnhart, W. D., Earle, P. S., & Benz, H. M. (2017). Oklahoma experiences largest earthquake during ongoing regional wastewater injection hazard mitigation efforts. *Geophysical Research Letters*, 44(2), 711–717. doi: 10.1002/2016GL071685
- Yeck, W. L., Weingarten, M., Mcnamara, D., & Bergman, E. A. (2016). Far-field pressurization likely caused one of the largest injection induced earthquakes by reactivating a large preexisting basement fault structure. *Geophysical Research Letters* (October), 198–207. doi: 10.1002/2016GL070861. Received
- Zeller, D., Jewett, J. M., Bayne, C., Goebel, E., O'Connor, H., & Swineford, A. (1968). The Stratigraphic Succession in Kansas. *Kansas Geological Survey Bulletin*, 189, 81.
- Zhang, X., Jeffrey, R. G., Wu, B., & Zhang, G. (2016). Modeling of Injection Induced Seismic Events. In *Spe asia pacific hydraulic fracturing conference*. doi: 10.2118/181793-MS
- Zhang, Y., Person, M., Rupp, J., Ellett, K., Celia, M. A., Gable, C. W., ... Elliot, T. (2013). Hydrogeologic controls on induced seismicity in crystalline basement rocks due to fluid injection into basal reservoirs. *Groundwater*, 51(4), 525–538. doi: 10.1111/gwat.12071
- Zoback, M. D., & Gorelick, S. M. (2012). Earthquake triggering and large-scale geologic storage of carbon dioxide. *Proceedings of the National Academy of Sciences*, 109(26), 10164–10168. doi: 10.1073/pnas.1202473109

Figure 1:

The model area (red box) was selected to encompass the a) KGS oil and gas database, b) the KCC (blue) and KDHE (orange) injection volume database, and c) USGS catalog of earthquakes.



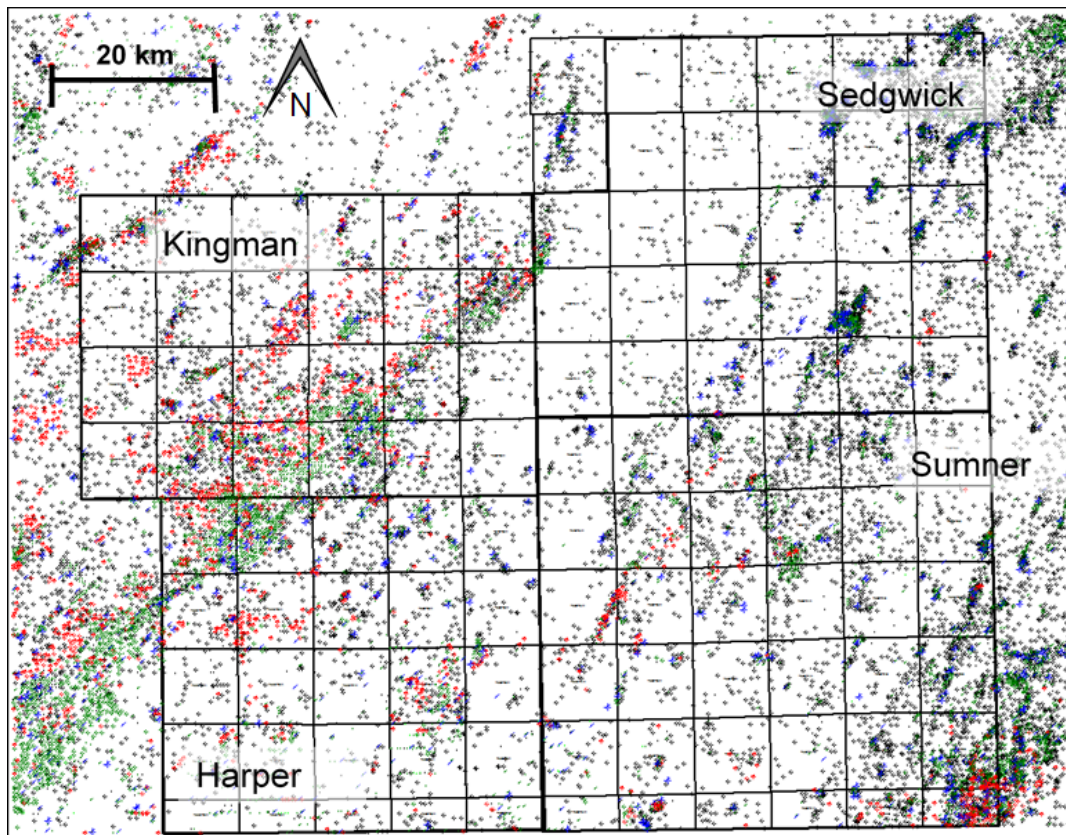


Figure 2:

29,601 well Locations where green indicates production wells, blue indicates injection wells, red indicates gas wells, and black indicates dry holes.

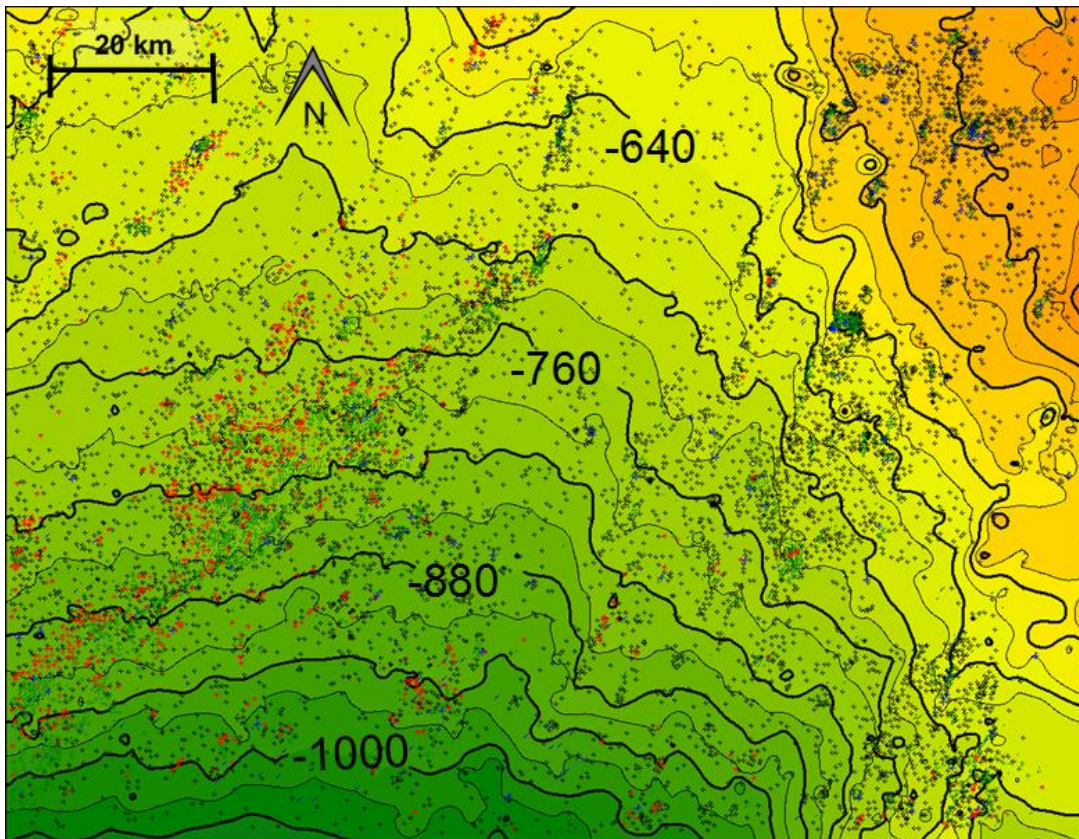


Figure 3:

Top Mississippian structure-contour map (meters) constructed using the identified 13,226 wells with a Mississippian formation top

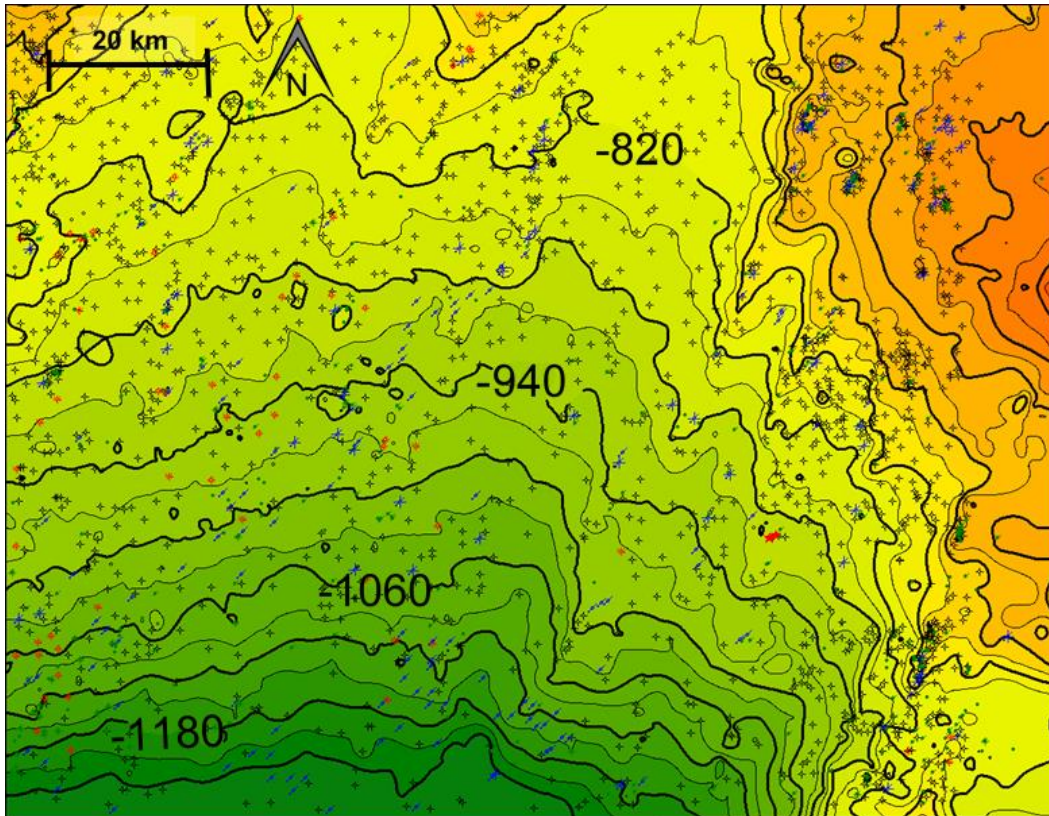


Figure 4:

Top Arbuckle structure-contour map (meters) constructed using the identified 2,100 wells with Arbuckle Formation Tops

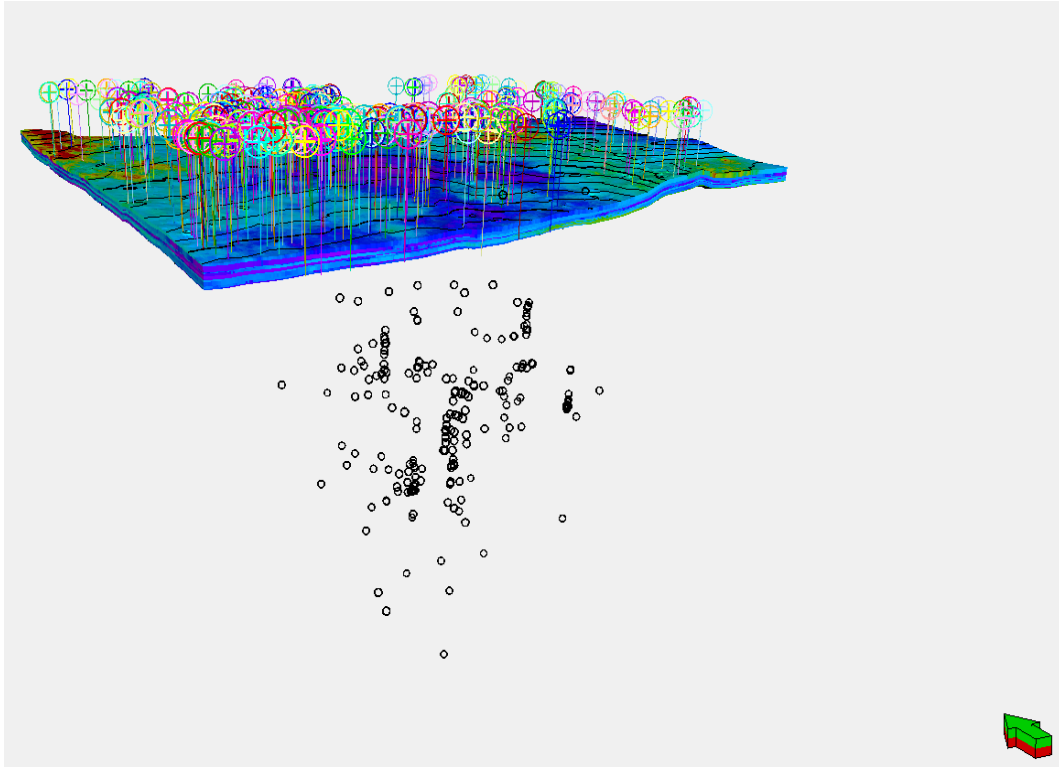


Figure 5:
The Arbuckle Model with 319 Arbuckle injection wells with injection (20x vertical exaggeration). The Arbuckle formation top is contoured on the top of the model. Earthquake hypocenters from 2014 of magnitude 2.5+ are identified at the recorded depth beneath the Arbuckle model.

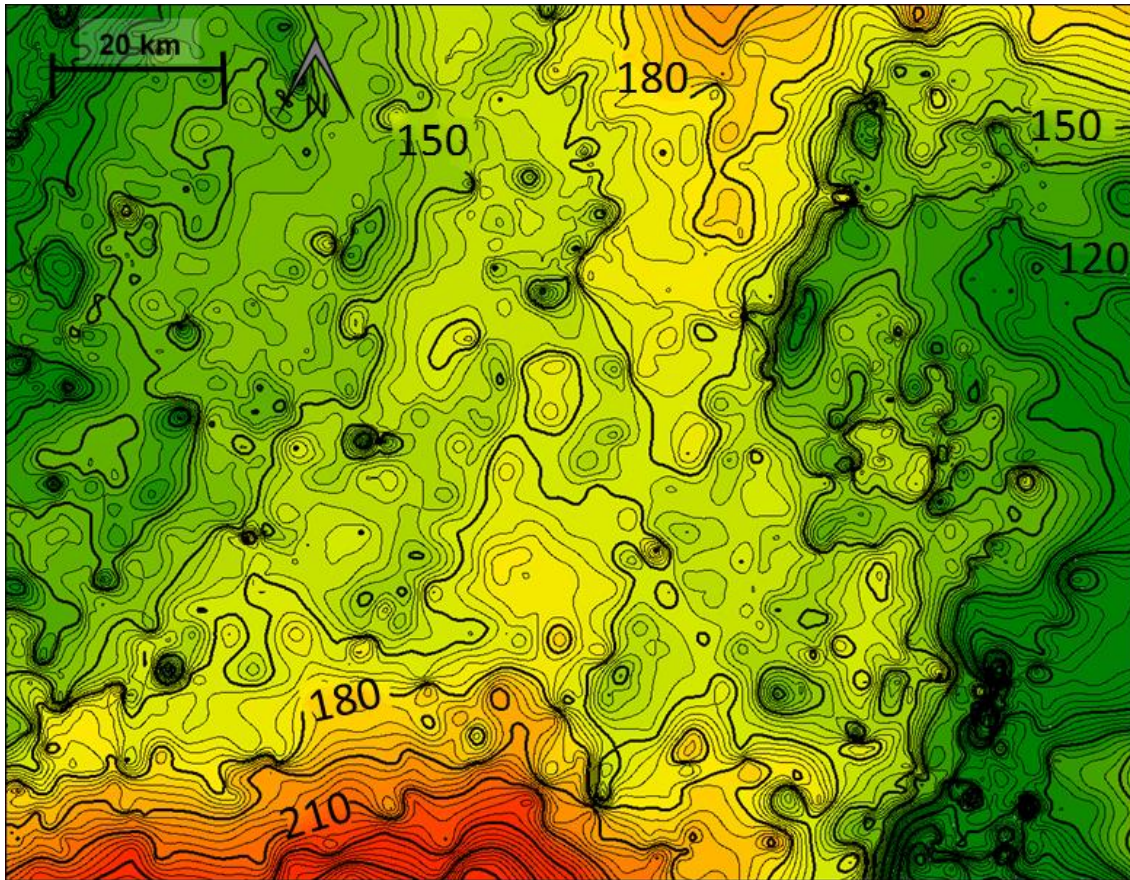


Figure 6:

Thickness between top of Mississippian and top of Arbuckle calculated by subtracting the Mississippian Structure grid from the Arbuckle structure grid presented on Figures 3 and 4, respectively.

Table 1: Cellular geometric statistics by layer.

Layer	Cells	Min Height (m)	Max Height (m)	Delta (m)	Mean (m)	Std (m)
1	133308	30.5	102.4	71.966328	71.2	12.4
2	133308	43.6	90	46.39056	49.5	4.7
3	132170	0	28.5	28.477464	14.9	7
4	133308	1.2	16.4	15.124176	8.4	3
5	133308	16.7	52.1	35.3568	28.5	6.4
6	73025	0	37.4	37.447728	12.7	7.6
7	33532	0	73	73.039224	9.2	8
8	127719	0	43.7	43.671744	27.8	9.8
9	118213	0	34.4	34.439352	17.7	8.3
10	133308	6.5	70.5	64.062864	32.8	11.4
11	129068	0	40.8	40.81272	21	10
12	133304	0	28.5	28.4988	10.4	4
Total	1413571	0	102.4	102.418896	27.1	20.1

Table 2: Statistical summary of five porosity realizations up-scaled from wireline log.

Property:	Porosity				
Unit:	%				
Data Source:	Wireline Log				
Upscale Method:	Random Gaussian Simulation				
Realization #:	1				
<u>Layer</u>	<u>Min</u>	<u>Max</u>	<u>Delta</u>	<u>Mean</u>	<u>Std</u>
1	1.3%	16.4%	15.1%	6.7%	2.6%
2	0.8%	6.0%	5.2%	3.8%	1.5%
3	0.4%	6.4%	6.0%	4.2%	1.8%
4	1.3%	8.9%	7.5%	4.9%	2.1%
5	2.3%	6.6%	4.2%	5.4%	1.3%
6	1.6%	8.2%	6.7%	5.1%	2.1%
7	1.9%	10.9%	9.0%	5.2%	2.6%
8	1.8%	8.1%	6.3%	4.3%	2.1%
9	3.1%	9.5%	6.5%	5.3%	1.8%
10	3.9%	10.5%	6.7%	6.5%	1.6%
11	1.5%	12.5%	10.9%	5.3%	2.8%
12	2.9%	10.1%	7.3%	5.3%	2.2%
Total	0.4%	16.4%	16.0%	5.2%	2.2%

Property:	Porosity				
Unit:	%				
Data Source:	Wireline Log				
Upscale Method:	Random Gaussian Simulation				
Realization #:	2				
<u>Layer</u>	<u>Min</u>	<u>Max</u>	<u>Delta</u>	<u>Mean</u>	<u>Std</u>
1	1.4%	16.4%	15.0%	7.1%	2.5%
2	0.8%	6.0%	5.2%	4.0%	1.4%
3	0.4%	6.4%	6.0%	4.3%	1.6%
4	1.3%	8.9%	7.5%	4.9%	2.2%
5	2.3%	6.6%	4.2%	5.0%	1.4%
6	1.6%	8.2%	6.7%	4.7%	2.1%
7	1.9%	10.9%	9.0%	5.6%	2.5%
8	1.8%	8.1%	6.3%	5.4%	2.0%
9	3.1%	9.5%	6.5%	6.1%	1.8%
10	3.9%	10.5%	6.7%	6.8%	1.7%
11	1.5%	12.5%	10.9%	5.9%	2.7%
12	2.9%	10.1%	7.3%	5.1%	1.6%
Total	0.4%	16.4%	16.0%	5.4%	2.2%

Property:	Porosity				
Unit:	%				
Data Source:	Wireline Log				
Upscale Method:	Random Gaussian Simulation				
Realization #:	3				
<u>Layer</u>	<u>Min</u>	<u>Max</u>	<u>Delta</u>	<u>Mean</u>	<u>Std</u>
1	1.4%	16.4%	15.0%	7.3%	2.4%
2	0.8%	6.0%	5.2%	4.1%	1.4%
3	0.4%	6.4%	6.0%	4.4%	1.6%
4	1.3%	8.9%	7.5%	4.7%	2.3%
5	2.3%	6.6%	4.2%	5.0%	1.4%
6	1.6%	8.2%	6.7%	4.0%	1.9%
7	1.9%	10.9%	9.0%	4.8%	2.3%
8	1.8%	8.1%	6.3%	5.2%	2.0%
9	3.1%	9.5%	6.5%	5.8%	1.8%
10	3.9%	10.5%	6.7%	6.6%	1.7%
11	1.5%	12.5%	10.9%	5.6%	2.8%
12	2.9%	10.1%	7.3%	5.1%	1.9%
Total	0.4%	16.4%	16.0%	5.3%	2.2%

Property:	Porosity				
Unit:	%				
Data Source:	Wireline Log				
Upscale Method:	Random Gaussian Simulation				
Realization #:	4				
<u>Layer</u>	<u>Min</u>	<u>Max</u>	<u>Delta</u>	<u>Mean</u>	<u>Std</u>
1	1.3%	16.4%	15.1%	6.8%	1.7%
2	0.8%	6.0%	5.2%	4.3%	1.3%
3	0.4%	6.4%	6.0%	4.5%	1.6%
4	1.3%	8.9%	7.5%	4.9%	2.4%
5	2.3%	6.6%	4.2%	5.0%	1.5%
6	1.6%	8.2%	6.7%	4.8%	2.4%
7	1.9%	10.9%	9.0%	6.8%	3.1%
8	1.8%	8.1%	6.3%	5.7%	2.2%
9	3.1%	9.5%	6.5%	5.9%	2.0%
10	3.9%	10.5%	6.7%	6.8%	1.8%
11	1.5%	12.5%	10.9%	5.8%	2.9%
12	2.9%	10.1%	7.3%	5.2%	1.8%
Total	0.4%	16.4%	16.0%	5.5%	2.2%

Property:	Porosity				
Unit:	%				
Data Source:	Wireline Log				
Upscale Method:	Random Gaussian Simulation				
Realization #:	5				
<u>Layer</u>	<u>Min</u>	<u>Max</u>	<u>Delta</u>	<u>Mean</u>	<u>Std</u>
1	1.9%	16.4%	14.6%	6.8%	1.8%
2	0.8%	6.0%	5.2%	4.2%	1.3%
3	0.4%	6.4%	6.0%	4.5%	1.6%
4	1.3%	8.9%	7.5%	5.2%	2.3%
5	2.3%	6.6%	4.2%	5.3%	1.3%
6	1.6%	8.2%	6.7%	5.5%	2.2%
7	1.9%	10.9%	9.0%	5.3%	2.5%
8	1.8%	8.1%	6.3%	6.1%	2.0%
9	3.1%	9.5%	6.5%	6.7%	1.8%
10	3.9%	10.5%	6.7%	7.4%	1.7%
11	1.5%	12.5%	10.9%	6.7%	2.9%
12	2.9%	10.1%	7.3%	5.6%	1.9%
Total	0.4%	16.4%	16.0%	5.8%	2.2%

Table 3: Statistical summary of five permeability realizations up-scaled from wireline log.

Property:	Permeability				
Unit:	mD				
Data Source:	Wireline Log				
Upscale Method:	Random Gaussian Simulation				
Realization #:	1				
<u>Layer</u>	<u>Min</u>	<u>Max</u>	<u>Delta</u>	<u>Mean</u>	<u>Std</u>
1	0.2	1.9	1.7	0.8	0.5
2	0.3	0.7	0.5	0.5	0.1
3	0.3	0.8	0.5	0.4	0.2
4	0.1	1.4	1.2	0.6	0.5
5	0.3	1.1	0.8	0.6	0.3
6	0.2	1.9	1.7	0.6	0.5
7	0.3	1.4	1.1	0.9	0.4
8	0.4	6.1	5.6	2.4	2.4
9	0.5	1.2	0.7	0.8	0.2
10	0.3	1.4	1.2	0.7	0.3
11	0.2	0.5	0.2	0.3	0.1
12	0.1	0.3	0.3	0.2	0.1
Total	0.1	6.1	6.0	0.7	0.9

Property:	Permeability				
Unit:	mD				
Data Source:	Wireline Log				
Upscale Method:	Random Gaussian Simulation				
Realization #:	2				
<u>Layer</u>	<u>Min</u>	<u>Max</u>	<u>Delta</u>	<u>Mean</u>	<u>Std</u>
1	0.2	1.9	1.7	0.8	0.6
2	0.3	0.7	0.5	0.5	0.2
3	0.3	0.8	0.5	0.5	0.2
4	0.1	1.4	1.2	0.7	0.5
5	0.3	1.1	0.8	0.7	0.3
6	0.2	1.9	1.7	0.9	0.8
7	0.3	1.4	1.1	1.0	0.4
8	0.4	6.1	5.6	2.7	2.5
9	0.5	1.2	0.7	0.9	0.3
10	0.3	1.4	1.2	0.8	0.5
11	0.2	0.5	0.2	0.4	0.1
12	0.1	0.3	0.3	0.2	0.1
Total	0.1	6.1	6.0	0.8	1.0

Property:	Permeability				
Unit:	mD				
Data Source:	Wireline Log				
Upscale Method:	Random Gaussian Simulation				
Realization #:	3				
<u>Layer</u>	<u>Min</u>	<u>Max</u>	<u>Delta</u>	<u>Mean</u>	<u>Std</u>
1	0.2	1.9	1.7	0.9	0.5
2	0.3	0.7	0.5	0.5	0.1
3	0.3	0.8	0.5	0.4	0.2
4	0.1	1.4	1.2	0.6	0.5
5	0.3	1.1	0.8	0.6	0.3
6	0.2	1.9	1.7	0.9	0.7
7	0.3	1.4	1.1	0.8	0.3
8	0.4	6.1	5.6	2.3	2.3
9	0.5	1.2	0.7	0.8	0.2
10	0.3	1.4	1.2	0.8	0.4
11	0.2	0.5	0.2	0.4	0.1
12	0.1	0.3	0.3	0.2	0.1
Total	0.1	6.1	6.0	0.7	0.9

Property:	Permeability				
Unit:	mD				
Data Source:	Wireline Log				
Upscale Method:	Random Gaussian Simulation				
Realization #:	4				
<u>Layer</u>	<u>Min</u>	<u>Max</u>	<u>Delta</u>	<u>Mean</u>	<u>Std</u>
1	0.2	1.9	1.7	1.1	0.5
2	0.3	0.7	0.5	0.5	0.1
3	0.3	0.8	0.5	0.4	0.2
4	0.1	1.4	1.2	0.5	0.5
5	0.3	1.1	0.8	0.6	0.3
6	0.2	1.9	1.7	0.8	0.7
7	0.3	1.4	1.1	0.7	0.3
8	0.4	6.1	5.6	2.1	2.3
9	0.5	1.2	0.7	0.9	0.2
10	0.3	1.4	1.2	0.8	0.4
11	0.2	0.5	0.2	0.4	0.1
12	0.1	0.3	0.3	0.2	0.1
Total	0.1	6.1	6.0	0.7	0.9

Property:	Permeability				
Unit:	mD				
Data Source:	Wireline Log				
Upscale Method:	Random Gaussian Simulation				
Realization #:	5				
<u>Layer</u>	<u>Min</u>	<u>Max</u>	<u>Delta</u>	<u>Mean</u>	<u>Std</u>
1	0.2	1.9	1.7	0.9	0.6
2	0.3	0.7	0.5	0.5	0.1
3	0.3	0.8	0.5	0.4	0.2
4	0.1	1.4	1.2	0.4	0.4
5	0.3	1.1	0.8	0.5	0.3
6	0.2	1.9	1.7	0.7	0.6
7	0.3	1.4	1.1	0.7	0.3
8	0.4	6.1	5.6	1.7	2.0
9	0.5	1.2	0.7	0.8	0.2
10	0.3	1.4	1.2	0.7	0.4
11	0.2	0.5	0.2	0.3	0.1
12	0.1	0.3	0.3	0.2	0.1
Total	0.1	6.1	6.0	0.6	0.8

Table 4: Statistical summary of five porosity realizations up-scaled from core analysis.

Property:	Porosity				
Unit:	%				
Data Source:	Core Analysis				
Upscale Method:	Random Gaussian Simulation				
Realization #:	1				
<u>Layer</u>	<u>Min</u>	<u>Max</u>	<u>Delta</u>	<u>Mean</u>	<u>Std</u>
1	1.9%	16.4%	14.6%	6.8%	1.8%
2	0.8%	6.0%	5.2%	4.2%	1.3%
3	0.4%	6.4%	6.0%	4.5%	1.6%
4	1.3%	8.9%	7.5%	5.2%	2.3%
5	2.3%	6.6%	4.2%	5.3%	1.3%
6	1.6%	8.2%	6.7%	5.5%	2.2%
7	1.9%	10.9%	9.0%	5.3%	2.5%
8	1.8%	8.1%	6.3%	6.1%	2.0%
9	3.1%	9.5%	6.5%	6.7%	1.8%
10	3.9%	10.5%	6.7%	7.4%	1.7%
11	1.5%	12.5%	10.9%	6.7%	2.9%
12	2.9%	10.1%	7.3%	5.6%	1.9%
Total	0.4%	16.4%	16.0%	5.8%	2.2%

Property:	Porosity				
Unit:	%				
Data Source:	Core Analysis				
Upscale Method:	Random Gaussian Simulation				
Realization #:	2				
<u>Layer</u>	<u>Min</u>	<u>Max</u>	<u>Delta</u>	<u>Mean</u>	<u>Std</u>
1	1.8%	8.9%	7.1%	6.3%	1.7%
2	1.8%	8.9%	7.1%	3.3%	1.7%
3	1.8%	8.8%	7.0%	3.1%	1.7%
4	1.8%	8.9%	7.1%	3.0%	1.7%
5	1.8%	8.9%	7.1%	4.3%	1.7%
6	1.8%	8.9%	7.1%	3.8%	1.7%
7	1.9%	8.3%	6.5%	3.2%	1.6%
8	1.8%	8.9%	7.1%	3.3%	1.7%
9	1.8%	8.9%	7.1%	4.4%	1.7%
10	1.8%	8.9%	7.1%	4.2%	1.7%
11	1.8%	8.9%	7.1%	3.9%	1.7%
12	1.8%	8.9%	7.1%	4.0%	1.7%
Total	1.8%	8.9%	7.1%	3.8%	1.9%

Property:	Porosity				
Unit:	%				
Data Source:	Core Analysis				
Upscale Method:	Random Gaussian Simulation				
Realization #:	3				
<u>Layer</u>	<u>Min</u>	<u>Max</u>	<u>Delta</u>	<u>Mean</u>	<u>Std</u>
1	1.8%	8.9%	7.1%	5.9%	1.8%
2	1.8%	8.8%	6.9%	2.8%	1.5%
3	1.8%	8.7%	6.9%	2.6%	1.5%
4	1.8%	8.7%	6.9%	2.5%	1.5%
5	1.8%	8.8%	7.0%	3.6%	1.6%
6	1.8%	8.8%	6.9%	2.8%	1.3%
7	1.8%	7.9%	6.0%	2.2%	0.7%
8	1.8%	8.8%	6.9%	2.8%	1.5%
9	1.8%	8.8%	7.0%	3.6%	1.7%
10	1.8%	8.8%	7.0%	3.5%	1.6%
11	1.8%	8.8%	7.0%	3.3%	1.6%
12	1.8%	8.8%	7.0%	3.3%	1.6%
Total	1.8%	8.9%	7.1%	3.2%	1.8%

Property:	Porosity				
Unit:	%				
Data Source:	Core Analysis				
Upscale Method:	Random Gaussian Simulation				
Realization #:	4				
<u>Layer</u>	<u>Min</u>	<u>Max</u>	<u>Delta</u>	<u>Mean</u>	<u>Std</u>
1	1.9%	8.9%	7.0%	6.5%	1.8%
2	1.8%	8.9%	7.1%	3.8%	2.3%
3	1.8%	8.9%	7.1%	3.6%	2.3%
4	1.8%	8.9%	7.1%	3.5%	2.3%
5	1.8%	8.9%	7.1%	4.6%	2.1%
6	1.8%	8.9%	7.1%	3.7%	2.1%
7	1.8%	8.9%	7.0%	2.9%	1.9%
8	1.8%	8.9%	7.1%	3.8%	2.3%
9	1.9%	8.9%	7.1%	4.7%	2.1%
10	1.8%	8.9%	7.1%	4.6%	2.1%
11	1.8%	8.9%	7.1%	4.2%	2.1%
12	1.8%	8.9%	7.1%	4.4%	2.1%
Total	1.8%	8.9%	7.1%	4.1%	2.3%

Property:	Porosity				
Unit:	%				
Data Source:	Core Analysis				
Upscale Method:	Random Gaussian Simulation				
Realization #:	5				
<u>Layer</u>	<u>Min</u>	<u>Max</u>	<u>Delta</u>	<u>Mean</u>	<u>Std</u>
1	1.8%	8.9%	7.1%	6.6%	2.0%
2	1.8%	8.8%	6.9%	3.2%	1.8%
3	1.8%	8.8%	6.9%	3.1%	1.8%
4	1.8%	8.8%	6.9%	2.9%	1.8%
5	1.8%	8.8%	7.0%	4.2%	1.8%
6	1.8%	8.8%	7.0%	3.7%	1.8%
7	1.8%	8.6%	6.7%	2.8%	1.4%
8	1.8%	8.8%	6.9%	3.2%	1.8%
9	1.8%	8.8%	7.0%	4.1%	1.8%
10	1.8%	8.8%	7.0%	4.1%	1.8%
11	1.8%	8.8%	7.0%	3.8%	1.7%
12	1.8%	8.8%	7.0%	3.8%	1.7%
Total	1.8%	8.9%	7.1%	3.7%	2.0%

Table 5: Statistical summary of five permeability realizations up-scaled from core analysis.

Property:		Permeability			
Unit:		mD			
Data Source:		Core Analysis			
Upscale Method:		Random Gaussian Simulation			
Realization #:		1			
<u>Layer</u>	<u>Min</u>	<u>Max</u>	<u>Delta</u>	<u>Mean</u>	<u>Std</u>
1	0.1	33.6	33.4	3.8	8.0
2	2.7	2.7	0.0	2.7	0.0
3	2.0	2.0	0.0	2.0	---
4	0.0	0.0	0.0	0.0	---
5	8.4	8.4	0.0	8.4	---
6	5.1	5.1	0.0	5.1	---
7	2.9	2.9	0.0	2.9	---
8	1.0	1.0	0.0	1.0	0.0
9	11.4	11.4	0.0	11.4	---
10	9.0	9.0	0.0	9.0	---
11	1.2	1.2	0.0	1.2	---
12	0.3	0.3	0.0	0.3	0.0
Total	0.0	33.6	33.5	4.0	4.4

Property:	Permeability				
Unit:	mD				
Data Source:	Core Analysis				
Upscale Method:	Random Gaussian Simulation				
Realization #:	2				
<u>Layer</u>	<u>Min</u>	<u>Max</u>	<u>Delta</u>	<u>Mean</u>	<u>Std</u>
1	0.1	33.6	33.4	10.2	12.0
2	2.7	2.7	0.0	2.7	0.0
3	2.0	2.0	0.0	2.0	---
4	0.0	0.0	0.0	0.0	---
5	8.4	8.4	0.0	8.4	---
6	5.1	5.1	0.0	5.1	---
7	2.9	2.9	0.0	2.9	---
8	1.0	1.0	0.0	1.0	0.0
9	11.4	11.4	0.0	11.4	---
10	9.0	9.0	0.0	9.0	---
11	1.2	1.2	0.0	1.2	---
12	0.3	0.3	0.0	0.3	0.0
Total	0.0	33.6	33.5	4.6	5.5

Property:	Permeability				
Unit:	mD				
Data Source:	Core Analysis				
Upscale Method:	Random Gaussian Simulation				
Realization #:	3				
<u>Layer</u>	<u>Min</u>	<u>Max</u>	<u>Delta</u>	<u>Mean</u>	<u>Std</u>
1	0.1	33.6	33.4	8.6	9.1
2	2.7	2.7	0.0	2.7	0.0
3	2.0	2.0	0.0	2.0	---
4	0.0	0.0	0.0	0.0	---
5	8.4	8.4	0.0	8.4	---
6	5.1	5.1	0.0	5.1	---
7	2.9	2.9	0.0	2.9	---
8	1.0	1.0	0.0	1.0	0.0
9	11.4	11.4	0.0	11.4	---
10	9.0	9.0	0.0	9.0	---
11	1.2	1.2	0.0	1.2	---
12	0.3	0.3	0.0	0.3	0.0
Total	0.0	33.6	33.5	4.4	4.8

Property:	Permeability				
Unit:	mD				
Data Source:	Core Analysis				
Upscale Method:	Random Gaussian Simulation				
Realization #:	4				
<u>Layer</u>	<u>Min</u>	<u>Max</u>	<u>Delta</u>	<u>Mean</u>	<u>Std</u>
1	0.1	33.6	33.4	4.8	8.5
2	2.7	2.7	0.0	2.7	0.0
3	2.0	2.0	0.0	2.0	---
4	0.0	0.0	0.0	0.0	---
5	8.4	8.4	0.0	8.4	---
6	5.1	5.1	0.0	5.1	---
7	2.9	2.9	0.0	2.9	---
8	1.0	1.0	0.0	1.0	0.0
9	11.4	11.4	0.0	11.4	---
10	9.0	9.0	0.0	9.0	---
11	1.2	1.2	0.0	1.2	---
12	0.3	0.3	0.0	0.3	0.0
Total	0.0	33.6	33.5	4.0	4.5

Property:	Permeability				
Unit:	mD				
Data Source:	Core Analysis				
Upscale Method:	Random Gaussian Simulation				
Realization #:	5				
<u>Layer</u>	<u>Min</u>	<u>Max</u>	<u>Delta</u>	<u>Mean</u>	<u>Std</u>
1	0.1	33.6	33.4	8.0	10.5
2	2.7	2.7	0.0	2.7	0.0
3	2.0	2.0	0.0	2.0	---
4	0.0	0.0	0.0	0.0	---
5	8.4	8.4	0.0	8.4	---
6	5.1	5.1	0.0	5.1	---
7	2.9	2.9	0.0	2.9	---
8	1.0	1.0	0.0	1.0	0.0
9	11.4	11.4	0.0	11.4	---
10	9.0	9.0	0.0	9.0	---
11	1.2	1.2	0.0	1.2	---
12	0.3	0.3	0.0	0.3	0.0
Total	0.0	33.6	33.5	4.4	5.0

Table 6: Statistical summary of five permeability realizations of up-scaled drill-stem-test.

Property:	Permeability				
Unit:	mD				
Data Source:	Drill Stem Test				
Upscale Method:	Random Gaussian Simulation				
Realization #:	1				
<u>Layer</u>	<u>Min</u>	<u>Max</u>	<u>Delta</u>	<u>Mean</u>	<u>Std</u>
1	3.3	2481.7	2478.4	135.2	291.8
2	3.2	2538.4	2535.2	634.9	661.1
3	7.6	2579.8	2572.2	1030.9	825.6
4	8.9	2575.7	2566.8	1075.0	763.6
5	3.3	2580.0	2576.7	1593.4	828.3
6	25.0	2580.0	2555.0	1819.4	756.4
7	25.5	2580.0	2554.5	1558.6	776.3
8	40.5	2580.0	2539.5	2031.6	644.0
9	12.2	2577.8	2565.6	1274.7	831.2
10	3.9	2563.2	2559.3	599.4	690.4
11	3.1	2559.5	2556.4	818.7	855.5
12	3.1	2579.5	2576.4	223.0	582.7
Total	3.1	2580.0	2576.9	908.7	925.2

Property:	Permeability				
Unit:	mD				
Data Source:	Drill Stem Test				
Upscale Method:	Random Gaussian Simulation				
Realization #:	2				
<u>Layer</u>	<u>Min</u>	<u>Max</u>	<u>Delta</u>	<u>Mean</u>	<u>Std</u>
1	3.5	2579.9	2576.4	555.3	784.5
2	8.3	2571.4	2563.0	1079.8	785.3
3	11.1	2577.1	2566.0	1046.1	786.9
4	11.8	2575.1	2563.3	1337.5	667.7
5	15.3	2580.0	2564.7	2033.2	672.2
6	23.1	2580.0	2556.9	1971.3	711.3
7	280.9	2580.0	2299.1	2320.8	453.1
8	31.9	2579.6	2547.7	2114.8	614.7
9	5.8	2568.9	2563.1	1193.8	748.5
10	5.8	2569.6	2563.8	1038.9	811.0
11	3.1	2578.4	2575.3	890.8	857.0
12	3.1	2573.9	2570.8	456.4	763.7
Total	3.1	2580.0	2576.9	1133.4	953.3

Property:	Permeability				
Unit:	mD				
Data Source:	Drill Stem Test				
Upscale Method:	Random Gaussian Simulation				
Realization #:	3				
<u>Layer</u>	<u>Min</u>	<u>Max</u>	<u>Delta</u>	<u>Mean</u>	<u>Std</u>
1	3.5	2579.9	2576.4	448.3	689.0
2	4.4	2571.5	2567.1	664.2	691.5
3	3.2	2577.5	2574.4	680.8	714.0
4	4.7	2579.1	2574.5	936.0	748.8
5	9.1	2580.0	2570.9	1595.2	853.9
6	27.3	2580.0	2552.7	1605.6	825.4
7	61.9	2580.0	2518.1	1991.6	772.6
8	5.4	2579.8	2574.4	1693.5	844.3
9	4.2	2579.8	2575.6	786.1	723.3
10	3.5	2577.2	2573.7	639.6	729.8
11	3.1	2566.5	2563.4	565.3	764.8
12	3.1	2575.2	2572.1	214.6	546.5
Total	3.1	2580.0	2576.9	812.1	888.3

Property:	Permeability				
Unit:	mD				
Data Source:	Drill Stem Test				
Upscale Method:	Random Gaussian Simulation				
Realization #:	4				
<u>Layer</u>	<u>Min</u>	<u>Max</u>	<u>Delta</u>	<u>Mean</u>	<u>Std</u>
1	3.7	2579.9	2576.2	489.6	737.8
2	5.1	2575.2	2570.1	886.0	805.9
3	3.7	2576.4	2572.7	896.9	782.9
4	3.5	2579.8	2576.3	1145.9	748.0
5	12.4	2580.0	2567.6	1797.8	781.0
6	9.5	2580.0	2570.5	1799.2	836.2
7	12.3	2580.0	2567.7	2248.0	636.4
8	9.3	2579.8	2570.5	1867.3	753.0
9	3.3	2572.3	2569.0	978.2	827.8
10	3.6	2572.8	2569.2	845.9	812.2
11	3.1	2578.2	2575.1	682.1	845.3
12	3.1	2560.5	2557.4	340.0	671.4
Total	3.1	2580.0	2576.9	970.8	944.6

Property:	Permeability				
Unit:	mD				
Data Source:	Drill Stem Test				
Upscale Method:	Random Gaussian Simulation				
Realization #:	5				
<u>Layer</u>	<u>Min</u>	<u>Max</u>	<u>Delta</u>	<u>Mean</u>	<u>Std</u>
1	3.2	2576.3	2573.1	517.4	772.7
2	11.1	2575.2	2564.1	1174.8	836.2
3	13.7	2574.9	2561.2	1141.8	843.8
4	27.8	2579.4	2551.6	1375.7	718.9
5	45.4	2580.0	2534.6	2021.3	688.1
6	87.3	2580.0	2492.7	2056.5	649.9
7	78.1	2580.0	2501.9	2275.0	647.6
8	50.1	2579.6	2529.5	2103.4	612.0
9	7.7	2572.1	2564.4	1188.2	837.8
10	10.4	2567.6	2557.2	1071.2	808.1
11	3.1	2576.5	2573.4	992.9	910.2
12	3.1	2565.3	2562.2	544.3	796.7
Total	3.1	2580.0	2576.9	1169.3	971.9